Crystal structures of glycoprotein D of equine alphaherpesviruses reveal potential binding sites to the entry receptor MHC-I

Viviane Kremling[1]*, Bernhard Loll[2], Szymon Pach[3], Ismail Dahmani[4], Christoph Weise[5], Gerhard Wolber[3], Salvatore Chiantia[4], Markus C. Wahl[2,6], Nikolaus Osterrieder[1,7], Walid Azab[1]*

[1] Institut für Virologie, Robert von Ostertag-Haus, Zentrum für Infektionsmedizin, Freie Universität Berlin, Berlin, Germany,

[2] Laboratory of Structural Biochemistry, Freie Universität Berlin, Berlin, Germany,

[3] Institute of Pharmacy (Pharmaceutical Chemistry), Freie Universität Berlin, Berlin, Germany,

[4] Universität Potsdam, Institut für Biochemie und Biologie, Potsdam, Brandenburg, Germany,

[5] BioSupraMol Core Facility, Bio-Mass Spectrometry, Freie Universität Berlin, Berlin, Germany

[6] Helmholtz-Zentrum Berlin für Materialien und Energie, Macromolecular Crystallography, Berlin, Germany

[7] Department of Infectious Diseases and Public Health, City University of Hong Kong, Kowloon Tong, Hong Kong

*Corresponding authors:

22 E-mail: walid.azab@fu-berlin.de (WA)

23 E-mail: viviane.kremling@fu-berlin.de (VK)

Abstract

Cell entry of most alphaherpesviruses is mediated by the binding of glycoprotein D (gD) to different cell surface receptors. Equine herpesvirus type 1 (EHV-1) and EHV-4 gDs interact with equine major histocompatibility complex I (MHC-I) to initiate entry into equine cells. We have characterized the gD-MHC-I interaction by solving the crystal structures of EHV-1 and EHV-4 gDs (gD1, gD4), performing protein-protein docking simulations, surface plasmon resonance (SPR) analysis, and biological assays. The structures of gD1 and gD4 revealed the existence of a common V-set immunoglobulin-like (IgV-like) core comparable to those of other gD homologs. Molecular modeling yielded plausible binding hypotheses and identified key residues (F213 and D261) that are important for virus binding. Altering the key residues resulted in impaired virus growth in cells, which highlights the important role of these residues in the gD-MHC-I interaction. Taken together, our results add to our understanding of the initial herpesvirus-cell interactions and will contribute to the targeted design of antiviral drugs and vaccine development.

Author summary

Equine herpesvirus type 1 (EHV-1) and type 4 (EHV-4) are endemic in horses and cause great suffering as well as substantial economic losses to the equine industry. Current vaccines do not prevent infections and treatment is difficult. A prerequisite for vaccine and drug development is an in-depth understanding of the virus replication cycle, especially the virus entry process in order to block the infection at early stages. Entry of alphaherpesviruses into the host cell is mediated by a set of virus envelope glycoproteins including glycoprotein D (gD) that triggers the internalization of the virus particle. The structure of gD and the interaction with the entry receptor equine major histocompatibility complex class I (MHC-I) remains elusive. Here, we solved the crystal structures of gD1 and gD4 that allowed us to

model virus-receptor interaction and to determine the key residues for virus entry. Alterations of these key residues impaired virus growth in cell culture. The overall structure of gD1 and gD4 shows classical features of other alphaherpesvirus gDs making it possible to gain further insights into human pathogens as well.

Introduction

One of the most essential steps for virus replication is the entry process into host cells. In herpesviruses, more specifically alphaherpesviruses, cell entry is a complex multistep process that requires a stepwise contribution of five out of twelve envelope glycoproteins, namely glycoprotein B (gB), gC, gD, and the heterodimer gH/gL [1]. Of these, gD is the (main) receptor-binding protein that interacts with the cell receptors and triggers the subsequent fusion process with cell membrane and/or uptake by endocytosis [2–4].

Equine herpesvirus type 1 (EHV-1) and EHV-4 use equine major histocompatibility complex class I (MHC-I) as an entry receptor, however, no details of the molecular binding mode are available [5–7]. Only few other viruses are known to utilize MHC molecules as binding receptors but not as entry receptors. Coxsackievirus A9 requires MHC-I and GRP78 as co-receptors for virus internalization [8], Simian virus 40 (SV40) binds to cellular MHC-I, however, MHC-I does not mediate virus entry [9,10]. The fiber knob of Adenovirus type 5 (AdV-5) binds to the α2 region of human leukocyte antigen (HLA) [11],and the functional gD homolog gp42 in Epstein-Barr Virus (EBV) binds to MHC-II to activate membrane fusion [12].

MHC-I seems to be an unlikely receptor for viral entry since it is present on all somatic cells [13] and therefore does not confer tissue specificity. Additionally, it is one of the most polymorphic mammalian proteins with 10 to 25% difference in the amino acid sequence [14,15]. Typically, MHC-I plays a crucial role in the adaptive immunity by presenting

proteolytically processed intracellular proteins on the cell surface to T-cells and natural killer cells [16]. In case of an infected cell, virus-derived peptides are presented and the recognition by T-cell receptor (TCR) initiates an immune response [17]. Although utilized by EHV-1 and EHV-4 as entry receptors, not all MHC-I genes support the entry of both viruses [5,7,18]. Interestingly, the residue A173 in the α2 region of MHC-I seems to be necessary but not enough to trigger virus entry [7,18,19].

EHV-1 and EHV-4 are important pathogens that cause great suffering in *Equidae* and other mammals and result in huge economic losses to the equine industry [20]. Efforts have been made to find efficient vaccines against both viruses [21]. However, the protection is usually limited in time and efficacy; frequent outbreaks occur also in vaccinated horses [22–25].

Here, we present crystal structures of free gD1 and gD4, which show a similar fold as other gD proteins from related viruses such as herpes simplex virus type 1 (HSV-1) (PDB-ID 2C36, [26], pseudorabies virus (PrV, PDB-ID 5X5V, 27), and bovine herpesvirus type 1 (BoHV-1, PDB-ID 6LS9, [27]. We further measured dissociation constants (in a micromolar range) for recombinant gD1/gD4 and C-terminally truncated gD4 binding to equine MHC-I by surface plasmon resonance spectroscopy (SPR). No increased binding affinity was observed for the truncated protein as was the case for gD of HSV-1, HSV-2, and PrV [28,29], suggesting a structurally different mode of binding during entry into host cells. Cell culture assays showed that recombinant gD1 and gD4 as well as truncated gD4 can inhibit viral replication *in vitro*, where again the truncated version did not perform better than the full-length protein. The crystal structures were further used for *in silico* docking analyses to equine MHC-I. Based on these docking positions, viral mutants with point mutations at position F213 or D261 were produced and displayed significant growth impairments which support the proposed mode of binding of gD1 and gD4 to MHC-I.

Results

Crystal structure of unbound EHV-1 and EHV-4 gD

Recombinant gD1 and gD4 lacking the transmembrane region were produced in insect cells, purified by affinity and size exclusion chromatography and used for crystallization experiments (Figure S 1 and Figure S 2). To evaluate the correct identity, sequence, and molecular mass of gD1, gD4, and equine MHC-I, mass spectrometry (MS) analysis was conducted. Recombinant equine MHC-I 3.1 (Eqca-1*00101) including a peptide (SDYVKVSNI) linked to the β2-microglobulin (β2m) region was produced in insect cells as well and purified in the same manner as gD1 and gD4.

To this point, molecular masses of gD1 and gD4 were determined only by SDS-PAGE and Western blotting. However, these techniques are known to often lead to an overestimation of the molecular mass [30]. Here we employed matrix-assisted laser desorption ionization-time of flight mass spectrometry (MALDI-TOF-MS) to analyze diluted recombinant protein. The proteins gD1, gD4 and the MHC-I α-chain contain a Tobacco Etch Virus (TEV) cleavage site and a His_6-tag (ENLYFQG-H_6) which contribute approximately 1675 Da to the molecular weight of the molecules (calculated with https://web.expasy.org/peptide_mass). Additionally, the residues EF (approximately 300 Da) originating from the *Eco-RI* restriction site, were detected by in-source-decay (ISD) in the recombinant proteins. A size of approximately 43078 Da for gD1, 43761 Da for gD4, 37779 Da for the α-chain of MHC-I and 13241 Da for β2m with its linker and attached peptide was determined (Figure 1 A-C). Excluding the molecular weight of the TEV cleavage site and the His_6-tag (1675 Da), this translates into a molecular weight of 41403 and 42086 Da for soluble gD1 and gD4, respectively (Table 1) and implies an approximate molecular weight of 49345 Da for the recombinant MHC-I molecule consisting of α-chain (36100 Da) and β2m with linker and peptide (13240 Da), and 48500 Da without the linker.

The difference between predicted and observed molecular masses is due to post translational modifications (PTMs) such as glycosylations which contribute approximately 4000-5000 Da

(Table 1). Further analysis of recombinant gD1, gD4, and MHC-I by ISD and tandem mass spectrometry (MS/MS) of in-gel digested Coomassie-stained proteins confirmed protein identities and presence of the correct N- and C-termini of gD1 and gD4 and N-terminus of MHC-I α-chain (Figure S 4 A, B, C).

A 2.45 Å resolution diffraction data set was collected for a gD1 crystal, and the gD1 structure (Figure 2 A) was determined using the structure coordinates of HSV-1 gD (protein data bank PDB-ID 2C36) for molecular replacement and refined to an R_{work} of 20.3% and R_{free} of 25.7% (Table 2, PDB-ID 6SQJ). The crystal structure of gD1 contains two gD molecules per asymmetric unit. In solution only the monomeric form was observed by size exclusion chromatography (SEC)-multi-angle static light scattering (MALS) (Figure S 5). Two ions interpreted as magnesium are trapped between the molecules and coordinated by residues E242 and D261 of both protein chains together with water molecules. The residues E32 to R38 and N281 to T348 could not be modeled due to a lack of electron density. N-linked glycosylations are visible at the predicted sites N20 and N28 [31] which are conserved between gD1 and gD4 but not in gDs of other alphaherpesviruses.

GlycoproteinD4 was crystallized with only one protein per asymmetric unit. The structure was determined at a resolution of 1.9 Å (Table 2, PDB-ID 6TM8, Figure 2 B) using the coordinates of gD1 structure for molecular replacement and refined to an R_{work} of 17.5% and R_{free} of 21.5% (Table 2). In total 244 residues could be modeled (R34 to R277).

In the structures of gD1 and gD4, six cysteines were found to form three disulfide bonds at sites conserved in members of the gD plolypeptide family: C87/C209, C126/C223, and C138/C147 [27,29,32]. The overall folds of gD1 and gD4 are very similar with a root-mean-square deviation (rmsd) of 0.7 Å for 220 common Cα atoms (Figure 2 C). The cores consist of a nine-stranded (A', B, C, C', C", D, E, F, and G) β-barrel, arranged in a typical V-like Ig fold, flanked by N- and C-terminal extensions with loops, α-helices (α1, α2, α3', and α3), and

small β-strands (str2-4). The termini in both structures point in opposite directions (Figure 2) and the unresolved C-termini are predicted to be unstructured by FoldIndex (https://fold.weizmann.ac.il/fldbin/findex).

Table 1: Predicted and measured molecular mass in Da of recombinant gD1, gD4 (aa 31-349), and equine MHC-I 3.1 α and β2m region with the uncleaved TEV site and His_6-tag. Theoretical masses were calculated using https://web.expasy.org/peptide_mass/ and the actual mass determined by matrix-assisted laser desorption ionization-time of flight mass spectrometry (MALDI-TOF-MS). Post-translational modifications like glycosylations account for the discrepancies between the predictions and measurements. NA: not applicable.

Molecule	**predicted**	**measured**	**without TEV and His6**
gD1	38216	43078	41403
gD4	38252	43761	42086
MHC-I α 1-3	33399	37779	36104
β2m (+linker and peptide)	13243	13241	NA

Table 2: Crystallographic data collection and model refinement statistics.

	gD1	**gD4**
PDB-ID	**6SQJ**	**6TM8**
Data collection		
Wavelength [Å]	1.0332	0.91841
Temperature [K]	100	100

Space group	$P2_12_12_1$	$P2_12_12_1$
Unit cell parameters		
a, b, c [Å]	71.9; 94.5; 101.3	73.1; 59.6; 69.7
α=β=γ [°]	90	90
Resolution range [Å]	50.00 - 2.24 (2.38 - 2.24) [a]	50.00 - 1.90 (2.01 - 1.90)
Reflections [a]	218509 (33751) [a]	138685 (10835)
Unique reflections [a]	33402 (5140)	23671 (1810)
Completeness [%][a]	99.1 (95.8)	95.6 (78.2)
Multiplicity [a]	6.5 (6.6)	5.9 (3.5)
Data quality[a]		
I/σ(I) [a]	11.71 (0.92)	8.96 (0.96)
Rmeas [%][a]	13.5 (199)	17.4 (126.8)
$CC_{1/2}$ [a]	99.8 (58.6)	99.5 (40.9)
Wilson B factor [$Å^2$]	53.3	32
Refinement gD1 gD4		
Resolution range [Å][a]	50.00 - 2.24 (2.33 - 2.24)	50.00 - 1.90 (2.01 - 1.90)
Reflections[a]	33399 (3181)	23642 (1792)
Test set (5%) [a]	1669 (159)	1182 (89)
R_{work} [%][a]	20.3 (33.8)	17.5 (30.0)
R_{free} [%][a]	25.7 (34.0)	21.5 (37.2)
Contents of Asymmetric Unit		
Molecules, residues, atoms	2; 477; 4049	1; 244; 2037
Mg^{2+}, GlcNAc molecules, glycerol	2; 5; -	-; -; 4
Water molecules	132	174
Mean Temperature factors [$Å^2$][b]		

All atoms	58.7	31.1
Macromolecules	58	30.4
Ligands	106.7	49.9
Water oxygens	53.5	36
RMSD from target geometry		
Bond length [Å]	0.007	0.012
Bond angles [°]	0.84	1.04
Validation statistics[c]		
Ramachandran plot		
Residues in allowed regions [%]	2.8	2.5
Residues in favored regions [%]	97.2	97.5
MOLPROBITIY clashscore[d]	3.23	3.9

[a] Data for the highest resolution shell in parenthesis

[b] Calculated with PHENIX [33]

[c] Calculated with MOLPROBITY [34]

[d] Clash score is the number of serious steric overlaps (> 0.4) per 1 000 atoms.

Comparison of gD1, gD4, and homolog structures

The amino acid sequence identity between EHV-1 and EHV-4 gDs is 76%, much higher than compared to HSV-1 (25%, GenBank AAK19597), PrV (34%, GenBank AEM64108) or BoHV-1 (31%, GenBank NP045370). While the global folds of gDs of these different viruses are very similar (Figure 3), the number and positions of α-helices differ. Compared to EHV-1 and EHV-4 gDs, there is an extra helix termed α1' present in PrV and BoHV-1 gDs. PrV gD has an exclusive α2' helix which cannot be observed in other gD structures elucidated so far. In HSV-1 and HSV-2 gDs, the α3' helix is missing but is present in EHV-1, EHV-4, PrV, and BoHV-1 gDs (Figure 3D). In HSV-1 and HSV-2 gDs, the α1 helix is split and the α3

177 helix is kinked in HSV-1 (Figure 3 D) which is not seen in the other known gD structures.
178 The six disulfide bonds C87/C209, C126/C223, and C138/C147 are conserved across EHV-1,
179 EHV-4, PrV, HSV-1, HSV-2, and BoHV-1 gDs, while the predicted and resolved
180 glycosylation sites in the crystal structure of gD1 and gD4 are only conserved between EHV-1
181 and EHV-4 (N52, N61, N297, N386) (Figure S 6). Between gD1 and gD4, also the
182 magnesium-coordinating residues seen in the gD1 monomer-monomer interface are
183 conserved.
184

185 ## Soluble gD1 and gD4 engage recombinant MHC-I with similar
186 ## binding affinities

187 gD-binding affinities of different alphaherpesviruses to their receptors are known to differ
188 greatly. For example, PrV gD binds human nectin-1 in the nanomolar range [35]. HSV-1 gD
189 interacts more weakly, in a micromolar range, with nectin-1 and herpesvirus entry mediator
190 (HVEM) [26] similarly to BoHV-1 gD with nectin-1 [27] (Table 3). For HSV-1, HSV-2, and
191 PrV gDs, it has been demonstrated that C-terminal truncation of the proteins increases the
192 binding affinities up to 100-fold (Table 3).
193

194 To study the interaction of soluble gD1 and gD4 with recombinant equine MHC-I, a surface
195 plasmon resonance (SPR) binding assay was conducted. α-chains together with β2m with
196 linked peptide of equine MHC-I 3.1 were produced in insect cells and purified by IMAC and
197 SEC (Figure S 1 and Figure S 2 D). Additionally, the receptor affinity of a C-terminally
198 truncated EHV-4 gD, $gD4_{36\text{-}280,}$ was tested. The truncated protein was produced in the same
199 manner as gD1 and gD4 originally with the goal to crystallize it because the flexible C-
200 terminus was suspected to hinder crystallization of gD1 and gD4. However, shortly after the
201 production of the truncated $gD4_{36\text{-}280,}$ crystal structures were obtained for both gD1 and gD4
202 proteins. Therefore, for $gD4_{36\text{-}280}$ only receptor binding kinetics were determined instead of

crystallizing it. Another truncated version, $gD4_{45-276}$, could not be produced in insect cells, suggesting that the protein failed to fold properly. Binding analyses for soluble gDs were conducted by using a protein dilution series in a range of 0 to 13 950 nM.

Dissociation constants (K_d^{app}) of 4000 ± 800 nM and 4400 ± 1200 nM were calculated for gD1 and gD4, respectively (Figure 4 A and B). The truncated gD4 version, $gD4_{36-280}$, exhibited a receptor binding affinity to MHC-I in the same order of magnitude (5300 ± 1200 nM; Figure 4 C-E).

Table 3: Comparison of dissociation constants (K_d^{app}) of alphaherpesviruses-gDs binding their respective receptors measured by SPR. SW = swine, BO = bovine, MHC-I = equine (Eqca-1*00101), nectin-1/HVEM = human. The C-terminal truncation of proteins is displayed in brackets under 'gD origin'. The upper part of the table represents full-length proteins, the bottom part truncated proteins.

gD origin	**Receptor**	**K_d (nM)**	**Reference**
EHV-1 (349)	MHC-I	4000 ± 800	This study
EHV-4 (349)	MHC-I	4400 ± 1200	This study
HSV-1 (306)	HVEM	3200 ± 600	[36]
HSV-1 (306)	HVEM	4000	[26]
HSV-1 (306)	nectin-1	2700 ± 200	[37]
HSV-1 (306)	nectin-1	1800	[26]
HSV-2 (306)	HVEM	1500	[36]
PrV (354)	nectin-1	130 ± 70	[35]
PrV (337)	nectin-1	191	[29]
PrV (337)	SW-nectin-1	301	[29]
BoHV-1 (301)	nectin-1	879 ± 101	[27]

BoHV-1 (301)	BO-nectin-1	341 ± 106	[27]
EHV-4 (280)	MHC-I	5300 ± 1200	This study
HSV-1 (285)	HVEM	37	[38]
HSV-1 (285)	HVEM	110	[26]
HSV-1 (285)	nectin-1	38	[39]
HSV-1 (285)	nectin-1	70	[26]
HSV-1 (285)	nectin-1	17.1	[40]
HSV-1 (285)	nectin-1	12.5	[28]
HSV-2 (285)	nectin-1	19.1	[28]
PrV (284)	nectin-1	16.1	[29]
PrV (284)	SW-nectin-1	18.4	[29]
BoHV-1 (274)	nectin-1	701 ± 68	[27]
BoHV-1 (274)	BO-nectin-1	489 ± 157	[27]

Recombinant gD1, gD4, gD436-280 can block cell surface MHC-I

To test whether recombinant gD1 and gD4 can bind to cell surface MHC-I and subsequently inhibit virus entry, blocking assays were performed. Equine dermal (ED) cells were incubated with the recombinant proteins ranging from 0 to 150 µg/ml (0 - 3.5 µM) for one hour on ice and subsequently infected with either EHV-1 or EHV-4 at a multiplicity of infection (MOI) of 0.1. Viruses expressing green fluorescent protein (GFP) [41,42] during early infection were used to monitor and analyze the infection levels by flow cytometry. A dose-dependent reduction of infection of up to 50% and 33% on average with 150 µg/ml protein was observed for gD1 and gD4, respectively (Figure 5 A and B).

Plaque reduction assays were performed by using a similar procedure. Here, 150 µg/ml of gD1, gD4, and $gD4_{36\text{-}280}$ were used and cells were infected with 100 plaque forming units

(PFU) of EHV-1 or EHV-4. In the presence of soluble gD1, plaque numbers were decreased on an average by 51% for EHV-1. For EHV-4, the infection was reduced by an average of 32% after blocking the cells with soluble gD4 recombinant protein. gD4 was also able to block the entry of EHV-1 by 40%. Likewise, gD1 reduced EHV-4 infection by 29%. In general, gD1 proved to be more efficient in blocking both virus infections. The gD4 variant lacking the C-terminal membrane-proximal residues, $gD4_{36\text{-}280}$, could inhibit EHV-4 infection more efficiently with an average of 46% and proved to be slightly more potent than the extracellular domain of gD4 (32%) (Figure 5 C).

Taken together, all recombinant gDs compete with viral native proteins. A dose-dependent reduction of infection was observed for gD1 and gD4. Notably, both recombinant gDs are able to efficiently block the entry of EHV-1 and EHV-4.

In silico modeling predicts gD1 and gD4 residues F213 and D261 as hot spots for MHC-I binding

No structures are available for gD1 or gD4 in complex with MHC-I. Therefore, protein-protein docking experiments were performed. Based on data from EHV-1 and EHV-4 mutational studies with diverse MHC-I genotypes it can be assumed that gD binds in close proximity to MHC-I A173 since genotypes with other residues at this position are highly resistant against infections [7,18]. Available crystal structures of equine MHC-I Eqca-N*00602 (1.18.7–6) and Eqca-N*00601 (10.18) [43] feature a glutamic acid and a threonine residue at position 173 in the α2 chain, respectively, and are known not to support EHV-1 and EHV-4 infection [7]. Additionally, they contain mouse instead of equine β2m. Therefore, for *in silico* modeling of gD1 and gD4 binding MHC-I, a homology model of MHC-I genotype 3.1 was constructed to reproduce the experimental setup from the *in vitro* assays. The α-chain template (PDB ID: 4ZUU [43] and target sequences showed 85% identity and 88% similarity allowing the development of a high confidence model. In the next step, we

248 built a homology model of equine β2m to achieve a physiological MHC-I state. The β2m
249 template (PDB ID: 4ZUU) and target sequences showed 63% identity and 82% similarity and
250 were therefore also highly suitable for homology modeling. The final homology models of the
251 α-chain and β2m contained no Ramachandran outliers [44] (Figure S 7). The calculated
252 backbone rmsd to the template amounted to 0.4 Å in each structure suggesting the correct
253 global fold of the model. All positions (101-164 and 203-259 in MHC-I and 25-80 in β2m)
254 and geometries of disulfide bonds considered typical for MHC were correct, suggesting a high
255 model quality. The final model structure was obtained after assembling both chains and
256 relaxing the homology model with a molecular dynamics (MD) simulation and used directly
257 for the gD docking.
258 As described in the Materials and Methods section (*in silico* modeling suggests low impact of
259 MHC-I peptide on gD-MHC-I binding), we initially identified gD residue D261 as a plausible
260 hot spot contacting R169 in a peptide-free MHC-I docking. In order to mimic the
261 experimental setup in a more realistic way, we inserted the peptide SDYVKVSNI into the
262 MHC-I homology model for docking. This nonapeptide binds in a cleft between α2 and α3
263 helices of MHC-I and was used in the cell-based assays. Since the peptide conformation is
264 strongly dependent on the peptide length [43], the peptide CTSEEMNAF from MHC-I
265 1.18.7–6 (PDB-ID: 4ZUU) was used to build a plausible model. The modeled peptide
266 SDYVKVSNI showed no steric clashes and exhibited reasonable bond geometries with a
267 negligible deviation of backbone atom positions (calculated backbone rmsd of 0.8 Å to the
268 template) (**Error! Reference source not found.**).
269 gD1 and gD4 were docked to the MHC-I homology model with the modeled peptide.
270 Subsequently, a structure showing initially identified contacts between MHC-I R169 and gD
271 D261 were searched. Since ionic interactions are considered important for long-range binding
272 partner recognition [45], it was assumed that this contact should be present in the protein-
273 protein-interaction (PPI). In total, five complexes for gD1 and 21 complexes for gD4,

respectively, were found to bind to MHC-I. All structures were visually inspected according to selection criteria outlined in Table 5 and one docking result was selected for each protein complex. The EHV-1 gD complex was one of the 3% best scored results and the EHV-4 gD complex was in the 11% top results suggesting that both docking solutions represent low-energy protein complexes. Both structures showed similar gD-MHC-I orientations (Figure 6 A, C) and recurring comparable contacts over the trajectories of MD simulations (**Error! Reference source not found.**).

Two contacts frequently observed between gD1 and MHC-I were identified using PyContact [46]. The first hot spot residue is D261 surrounded by the assumed O-ring including residues F213 and W257 which are contacting MHC-I binding pocket residue R169. The second hot spot residue is F213 surrounded by the assumed O-ring including Y108 and N110 and contacting MHC-I binding pocket residue I166. Additionally, an extensive hydrogen bond network between residues R103 – E242 and E113 – R238 (Figure 6, B and D) was detected (MHC-I – gD residues, respectively). All contacts and their frequencies over the trajectory of MD simulations are summarized in **Error! Reference source not found.**.

PPIs over the course of MD simulations revealed minor movements measured as backbone rmsd of maximal 3.5 Å and 6.5 Å (gD1 and gD4, respectively; **Error! Reference source not found.**C and D). Based on the optimized docking models, two gD variants were designed for experimental validation in the next step: F213A and D261N. Both residue exchanges are predicted to disrupt gD – MHC-I contacts and lead to inhibition of viral replication in a cell-based assay.

Mutating F213A and D261N in EHV-1 and 4 gD leads to growth defects

The gD1/4-MHC-I binding hypotheses (Figure 6) were experimentally investigated by mutating the proposed key residues F213 to alanine and D261 to asparagine in EHV-1 and

EHV-4 gDs. Two-step Red-mediated mutagenesis [47] was performed on EHV-1 and EHV-4 bacterial artificial chromosomes (BACs) and multi-step growth kinetics with plaque reduction assays were used for virus characterization.

All mutant viruses were successfully reconstituted from mutated BACs and the modified gD gene sequences were confirmed by Sanger sequencing. EHV-1-gD$_{F213A}$ displayed a significant 2-log reduction in growth kinetics and low titers in cell supernatant compared to the parental virus. Reverting the mutation rescued virus growth in cell culture (Figure 7 B). Plaque sizes of wild type, mutant and revertant viruses were similar. The virus mutants EHV-1-gD$_{D261N}$, EHV-4-gD$_{D261N}$ and EHV-4-gD$_{F213A}$ did not grow in cells to the extent where growth kinetics could be analyzed. However, reverting the residue exchange in EHV-1-gD$_{D261N}$ rescued virus growth (Figure 7 A). Taken together, the gD$_{D261N}$ and gD$_{F213A}$ variants lead to replication-deficient viruses in EHV-1 and EHV-4.

Discussion

Although details of cell entry of alphaherpesviruses can differ greatly between virus species, four common steps characterize the whole entry processes. First gB and/or gC attach in a relatively unspecific and reversible manner to cell surface heparan sulfate proteoglycans (HSPG) and chondroitin sulfate proteoglycans (CSPG) [48–50]. This charge-based interaction is stabilized by a stronger and specific receptor-ligand interaction [51] followed by a signaling cascade which is activated by gD and gH/gL [52]. The latter process leads ultimately to the fusion of the viral envelope with the cell membrane or in some cases to entry via endocytosis through gB [4,53], gD is the essential protein that, in case of EHV-1 and EHV-4, binds to equine MHC-I [5–7]. The mode of gD binding to MHC-I remains elusive, although the structural understanding of alphaherpesviral gDs binding to their putative receptors has been largely extended in the last years [26,27,29,32]. Here, we present crystal structures of EHV-1

and EHV-4 gDs and propose a binding model to equine MHC-I through the key residues F213 and D261.

The crystal structures of EHV-1 and EHV-4 gDs revealed an IgV-like fold with large N- and C-termini wrapping around the core which is common for members of the gD polypeptide family. Despite high variability in sequence identities, the overall structure of alphaherpesviral gDs is conserved with only small variations in the loop regions and number of helices [26,27,29,32]. The gD termini have been shown to be important for the entry process in HSV-1 [26]. To allow receptor binding, the C-terminus needs to be displaced to free the N-terminal binding site. This could be a mechanism to prevent early onset of the fusion process before the ligand and receptor are in proximity. Subsequently, the displacement of the C-terminus allows the formation of an N-terminal hairpin loop that is crucial for HVEM binding, since exclusively gD N-terminal residues (7-15 and 24-32) interact with the receptor [26,32,54]. The displacement of the C-terminal tail is also needed for the complex formation with nectin-1 as the binding sites overlap with those of HVEM with additional C-terminal interactions (residues 35–38, 199–201, 214–217, 219–221, 223) [55]. The formation of an N-terminal loop is not involved in nectin-1 binding since the deletion of residues 7-32 had little impact on the interaction [56]. The N-terminus of gD1 and gD4 is, similarly to PrV gD, shorter than in HSV-1 gD, suggesting that HVEM cannot function as an entry receptor in these viruses. In fact, it has already been experimentally observed that HVEM is not used as entry receptors by PrV [29]. Similarly, we observed that EHV-1 also does not employ the equine HVEM homolog either [53]. In HSV-1, gD forms a dimer in the unbound state on the virus envelope [57]. This is thought to stabilize the C-terminus since viruses with a destabilized terminus could not efficiently enter cells. Although the ionic contact and high Complex Formation Significance Score of the here solved EHV-1 gD dimer interface suggest a similar function, no dimer was observed in SEC, SEC-MALS, and MS analysis. Therefore, we suppose that gD1 has no dimeric form on the virus envelope.

In contrast to results from C-terminally truncated gD homologs, which display a dramatic increase in receptor affinity (Table 3), truncated $gD4_{36-280}$ binds MHC-I similarly as the non-truncated version. The higher affinities in the truncated homologs are explained by a faster interaction with the receptors, since the C- terminus that blocks the binding site is not required to be displaced upon binding anymore [58]. That the C-terminal truncation had no significant effect on the receptor affinity of EHV-4 gD suggests that the mode of binding differs from other alphaherpesviruses. Taking into account that EHV-1 and EHV-4 bind to MHC-I instead of HVEM or nectin-1, a different binding mechanism would be assumed. In line with $gD4_{36-280}$, truncated BoHV-1 gD interaction with nectin-1 showed no increased receptor affinity [27] (Table 3). A conformational change in the loop region between the G-strand and α2 helix is needed for receptor binding [27] and might explain why the affinity of the truncated BoHV-1 gD does not increase.

SPR analysis showed binding of recombinant gD1, gD4, and $gD4_{36-280}$ to recombinant MHC-I with micromolar affinities. The K_d^{app} are higher than in gD homologs of HSV-1, HSV-2, and PrV binding nectin-1. However, HSV-1 gD binding to HVEM displays similar affinities (Table 3 upper part). Nevertheless, there are two limitations of the SPR analysis in this study. First, the MHC-I molecule Eqca-1*00101 (3.1) used here allowed lower infection rates in a previous study than the molecule Eqca-16*00101 (2.16) [7]. Due to construct design reasons, the gene 3.1 fitted the purpose of crystallography better, although, no crystal structure could be obtained. However, the 2.16 molecule should display higher receptor affinities than the one observed in this study. Second, the linker region (GGGSGGGSGGGS), inserted to tether the peptide in the MHC-I complex to the β2m C-terminus, might interfere with gD receptor binding. Our attempt to model the linker to the MHC-I molecule that binds gD1 in the position hypothesized here support this hypothesis. Nevertheless, the results from blocking assays confirm that the receptor affinities of soluble gDs are unlikely to be in the nanomolar range. Furthermore, blocking assays revealed that gD1, gD4, and $gD4_{36-280}$ can block cell

surface MHC-I and thus compete with native gD in the viral envelope. It could be demonstrated that gD1 can block EHV-4 infections and vice versa implying that the receptor interaction is very similar in both viruses. This finding is supported by the binding models presented here.

The finding in SPR analysis that the C-terminally truncated gD4 does not display an increased receptor affinity was confirmed in blocking assays, thus suggesting that the receptor-binding mode differs from HSV and PrV, which is not surprising as they enter through different receptors.

The proposed docking position of gD1 to MHC-I explains why MHC-I Eqca-16*00101 (2.16) allows higher infection rates than Eqca-1*00101 (3.1) [7]. The residue 103 in the 3.1 α1 region is an arginine, which is more spacious than asparagine in 2.16, thus preventing a closer interaction with gD and leading to lower receptor binding affinities. A binding hypothesis with MHC-I 2.16 and a crystal structure of this molecule could confirm that theory. A173 of MHC-I has been shown previously to play a major role in the entry of EHV-1 and EHV-4 by two studies. First, the entry of EHV-1 into usually non-susceptible NIH3T3 cells transfected with altered hamster MHC-I Q173A has been shown together with the negative effect on infection rates of hydroyphilic residues at position 173 in equine MHC-I [18]. Second, it has been demonstrated that not all equine MHC-I genes support entry of EHV-1 and 4 into equine MHC-I transfected mouse mastocytoma (P815) cells and that MHC-I genes harboring residues other than alanine at position 173 are highly resistant against EHV-1 and 4 infections [7]. The gD1/4-MHC-I binding hypotheses explain the role of MHC-I A173 well by showing that bulkier amino acids at that position lead to steric hindrance in the gD binding pocket. This applies to MHC-I alleles 3.3 (V173), 3.4 (T173), 3.5 (E173), and 3.6 (V173), which do not support EHV-1 and 4 entry [7,18]. The model can even explain why the genotype Eqca-7*00201 (3.7), although harboring an alanine at position 173, does not allow entry of EHV-1 and 4 into P815 3.7 [7]. The glutamine residue at position 174 is assumed to hinder gD

401 binding sterically. The side-chain would point in the bound state into a hydrophobic residue-
402 patch (W253, F256, W257) of gD, leading to an enthalpic penalty. Strangely, the inability of
403 the viruses to enter via the MHC-I haplotype Eqca-2*00101 (3.2) which harbors A173 and
404 A174 cannot be explained by the binding model. The topology of this MHC-I molecule is
405 predicted to be very similar to those allowing virus entry. A crystal structure of the 3.2 MHC-I
406 gene might give an explanation. Mutations in the gD binding pocket R43, W253, F256, and
407 W257 could prove useful for a more detailed evaluation of the predicted interaction with
408 MHC-I A173.
409 Another observation by Sasaki et al. [18] was that the mutation W171L in equine MHC-I
410 impairs virus entry into NIH3T3 cells transfected with this MHC-I. Although the cell surface
411 expression of this mutant was reduced, this is still interesting since structural data show that
412 W171 points towards the peptide in the binding groove and should therefore not be involved
413 directly in binding gD. The tryptophan would be able to stabilize some peptides with hydrogen
414 bonds, whereas a leucine would not. A leucine at position 171 could therefore lead to a
415 more loosely bound peptide with a higher flexibility, resulting in an interference via the gD-
416 MHC-I binding. This theory would suggest that the peptide in the MHC-I binding groove
417 itself could play a role in the receptor-ligand interaction, which could be tested by using
418 different peptides bound to MHC-I in blocking assays and by testing mutated equine MHC-I
419 W171L in blocking assays with soluble recombinant gDs.
420 Considering all these results, the question arises whether EHV-1 and EHV-4 can facilitate entry
421 through, so far, unknown non-equine MHC-I molecules. Sasaki et al. [18] demonstrated that
422 mutated hamster MHC-I Q173A allowed low EHV-1 infection. Unfortunately, EHV-4 has not
423 been tested in the same manner. A computational approach could be employed to search for non-
424 equine MHC-I molecules that are similar in the binding region that is visible in the gD1/4-MHC-
425 I binding model and be used to select promising targets for transfection/infection assays.
426 Experimentally, EHV-1 and EHV-4 infections could be tested in cell lines from susceptible

427 species, e.g. bovine, rabbit, monkey, pig, cat, human [59,60], alpacas, lamas, polar bears [61],
428 and rhinoceros [61–63] cell lines, with and without inhibited MHC-I expression by using β2m
429 knockdown as in Sasaki et al. [6].
430 Taken together, the proposed docking modes of gD1 and gD4 to MHC-I can explain several
431 experimentally obtained results and are therefore plausible. Additionally, the docking models
432 are supported by EHV-1 and EHV-4 viruses with mutated gD_{F213A} and gD_{D261N} that all
433 exhibited an impaired growth. A limitation in this experiment was the difficulty of reverting
434 EHV-4 mutations to original status to confirm that the observed effect was exclusively due to
435 the gD_{F213A} and gD_{D261N} variants. Nevertheless, it could be shown that the gD residues F213
436 and D261 play a key role during entry of EHV-1 and EHV-4 providing starting points for
437 further mutational studies possibly leading to an efficient vaccine. The results presented here
438 might also be used to generate gD-based EHV-1 and EHV-4 inhibitors for reduction of clinical
439 symptoms in horses and non-definite hosts.
440

441 # Materials and Methods

442 ## Viruses

443 EHV-1 strain RacL11 and EHV-4 strain TH20p are maintained as bacterial artificial
444 chromosome infections clones (BAC). The viruses have GFP under the control of the HCMV
445 major immediate-early (IE) promoter inserted into the Mini-F sequence to easily recognize
446 infected cells. Clones were generated as described previously in Rudolph et al. and Azab et al.
447 [41,42,64]. The viruses were grown on equine dermal (ED) cells (CCLV-RIE 1222, Federal
448 Research Institute for Animal Health, Greifswald, Germany) at 37 °C under a 5% CO2
449 atmosphere.
450

451 ## Cells

ED cells were grown in Iscove's modified Dulbecco's medium (IMDM; Pan, Biotech, Aidenbach, Germany) containing 20% fetal bovine serum (FBS; Biochom GmBH, Berlin, Germany), 1 mM sodium pyruvate (Pan Biotech, Aidenbach, Germany), 1% nonessential amino acids (NEAA; Biochom GmBH, Berlin, Germany), and P-S solution (100 U/mL penicillin: Panreac, AppliChem GmBH, Darmstadt, Germany; 100 µg/mL streptomycin: Alfa Aesar, Thermo Fisher Scientific, Kandel, Germany (P-S) at 37°C under a 5% CO2 atmosphere.

Human embryonic kidney (293T, ATCC CRL-11268) cells were propagated in Dulbecco's modified Eagle's medium (DMEM; Biochom GmBH, Berlin, Germany), supplemented with 10% FBS and P-S. Sf9 cells (IPLB-Sf21-AE, Invitrogen, Germany) were propagated in serum free Sf-900 III medium (Gibco, Thermo Fisher Scientific, New York, USA) and High Five™ cells (BTI-TN-5B1-4, Invitrogen, Germany) in serum free Express Five medium (Gibco, Thermo Fisher Scientific, New York, USA) at 27°C on orbital shaker.

Construction of expression plasmids

Constructs were amplified from insect cell codon-optimized DNA fragments (Bio Basic Inc., Canada) for protein production in High Five insect cells. Synthetic truncated genes contained the gene of interest (gD1 residues 32-249, gD4 residues 32-249, equine MHC-I 3.1,), a C-terminal TEV protease cleavage site (ENLYFQG), and a hexa-histidine tag (His_6), all flanked by *Eco*RI- and *Sca*I-restriction sites (Figure 8). Sequences of codon optimized genes can be found in the supplementary data. A further truncated form of gD4 containing the residues 36-280 was amplified from gD4 synthetic gene with the primer pair VK50/VK56 (**Error! Reference source not found.**).

The Autographa californica nuclear polyhedrosis virus (AcNPV) baculovirus gp64 signal sequence under control of the very late polyhedrin promoter was inserted into the insect cell vector plasmid pACEBac1 (Addgene, LGC Standards Teddington, UK) by using another

478 synthetic gene (VK18, LGC Genomics, Berlin, Germany) and the primer pairs VK7/VK7
479 (**Error! Reference source not found.**). Subsequently, plasmids containing synthetic genes
480 (gD1, gD4, MHC-I) were amplified in *Escherichia coli* (E. coli), purified, and digested with
481 *Eco*RI- and *Sca*I-restriction enzymes for insertion into the transfer vectors which was digested
482 with the same restriction enzymes. After ligation, these plasmids were transformed into
483 DH10MultiBac electrocompetent cells and recombinant baculoviruses produced according to
484 manufacturer's instructions (Bac-to-Bac expression system, Invitrogen). All constructs were
485 verified by sequencing (VK8 or VK10/WA2, VK35/38; **Error! Reference source not**
486 **found.**). Recombinant BACs were isolated and used for virus production in Sf9 cells as
487 described in Santos et al. [65].

488 # Protein production and purification

489 Equine MHC-I, $gD1_{32-349}$, $gD4_{32-349}$, and $gD4_{36-280}$ were expressed in HighFive cells. Cell
490 supernatant was harvested after 72 h post infection by centrifugation. The pH was adjusted to
491 7 with 1M tris(hydroxymethyl)aminomethan (Tris)-HCl buffer at pH 9 on ice and incubated
492 for at least 1 h with washed Ni^{2+}-NTA beads for affinity chromatography. Beads with bound
493 recombinant protein were collected by a gravity flow column and the proteins were eluted
494 with a buffer containing 20 mM Tris-HCl at pH 7.5 or 2-(N-morpholino)ethanesulfonic acid
495 (MES) at pH 6 for gDs and MHC-I, respectively, and 200 mM NaCl, 5% glycerol, and 200
496 mM imidazole. Concentrated protein was loaded onto a 16/600 Superdex 200 gel filtration
497 column (GE Healthcare Piscataway, NJ). The buffer conditions were the same as in Ni^{2+}-NTA
498 affinity chromatography but with 20 mM NaCl and no imidazole. Proteins collected from
499 size-exclusion chromatography were concentrated (Concentrators, Amicon Ultra, Millipore,
500 Darmstadt, Germany), aliquoted and directly used for crystallization or stored at −80°C.
501

Crystallization, structure determination, and refinement

Crystals of EHV-1 gD were obtained by the sitting-drop vapor-diffusion method at 18°C with a reservoir solution composed of 0.1 M Tris/HCl buffer at pH 8.5, 0.2 M MgCl, and 30% (w/v) polyethylene glycol (PEG) 4000. Crystals were cryo-protected with a solution composed of 75% mother liquor and 25% (v/v) glycerol and subsequently flash-cooled in liquid nitrogen. Synchrotron diffraction data were collected at the beamline P14 at DESY (Hamburg, Germany) and at the beamline 14-2 of the MX beamline of the BESSY II (Berlin, Germany) and processed with X-ray detector software (XDS) [66]. The structure was solved by molecular replacement with PHASER [67] using the coordinates of PDB-ID 2c36 as search model for gD1 which was then used as search model for gD4. A unique solution with two molecules in the asymmetric unit for gD1 and molecule for gD4 were subjected to the program AUTOBUILD in PHENIX [33] and manually adjusted in COOT [68]. The structures were refined by maximum-likelihood restrained refinement using PHENIX [33,69]. Model quality was evaluated with MolProbity [70] and the JCSG validation server [71]. Secondary structure elements were assigned with DSSP [72] and for displaying sequence alignments generated by ClustalOmega [73] ALSCRIPT [74] was used. Structure figures were prepared using PyMOL [75]. Coordinates and structure factors have been deposited in the PDB for gD1 with PDB-ID 6SQJ as well as for gD4 with PDB-ID 6TM8. Diffraction images have been deposited at proteindiffraction.org (gD1: DOI 10.18430/m36sqj and gD4 DOI 10.18430/m36tm8).

Mass spectrometry analysis

Intact protein mass of gD1, gD4, and MHC-I was determined by matrix-assisted laser desorption ionization-time of flight mass spectrometry (MALDI-TOF-MS) using an Ultraflex-II TOF/TOF instrument (Bruker Daltonics, Bremen, Germany) equipped with a 200 Hz solidstate Smart beam™ laser. Samples were spotted using the dried-droplet

technique on sinapinic acid (SA) or 2,5-dihydroxybenzoic acid (DHB) matrix (saturated solution in 33% acetonitrile / 0,1% trifluoroacetic acid). The mass spectrometer was operated in the positive linear mode, and spectra were acquired over an m/z range of 3,000-60,000. Data was analyzed using FlexAnalysis 2.4. software provided with the instrument. Protein identity was determined by tandem mass spectrometry (MS/MS) of in-gel digested Coomassie stained protein with 12,5µg/ml Glu-C and trypsin, and 10µg/ml Asp-N in 25nm ammonium bicarbonate.

N-terminal c and C-terminal (z+2) sequence ion series were generated by in-source decay (ISD) with 1,5-diaminonaphthalene (1,5-DAN) as matrix (20 mg/ml 1,5-DAN in 50% acetonitrile / 0,1% trifluoroacetic acid). Spectra were recorded in the positive reflector mode (RP PepMix) in the mass range 800–4,000.

SEC-MALS analysis

For molecular mass determination of soluble, recombinant gD1, SEC-MALS [76] was performed. Protein solution was run at room temperature on a Superdex 75 10/300 GL (GE Healthcare, Piscataway, NJ) column with 2 mg/ml gD1 and a mobile phase composed of Tris-HCl at pH 7.5, 200 mM NaCl, 5% glycerol, and 0.02% sodium azide, attached to a high-performance liquid chromatography (HPLC) system (Agilent Technologies, Santa Barbara, CA, USA) with a mini DAWN TREOS detector (Wyatt Technology Corp., Santa Barbara, CA, USA). Data was acquired and analyzed with the ASTRA for Windows software package (version 6.1.2).

Surface plasmon resonance

Binding kinetics of soluble gD1, gD4, and $gD4_{36\text{-}280}$ binding to amine-coupled recombinant, equine MHC-I 3.1 were measured at 25˚C on a surface plasmon resonance (SPR) GE Biacore J Biomolecular Interaction Analyser instrument (Uppsala, Sweden) using a polycarboxylate

hydrogel sensor chip HC200M (XanTec bioanalytics GmbH). The second channel was coated with poly-L-lysine and positive nanogels (size 214nm) [77] that were shown to interact only weakly with gDs and used as negative control. The control sensorgrams were subtracted from reaction sensorgrams and normalized. The surfaces were regenerated with buffer containing 200 mM NaCl and 10 mM NaOH after each cycle. Serial dilutions of gDs ranging from 0 to 10000 nM were injected at medium flow and the interaction with MHC-I was monitored for 15 min. The response curves of gDs binding to the MHC-I were fitted to the Hill-Wand binding model $R_{eq} = \frac{R_{max}[A]^b}{K_D^b + [A]^b}$ [78] using Sigma plot 12.0 software.

Generation and analysis of gD1/4-MHC-I binding model

Protein data

Sequences of MHC-I and β2m were obtained from UniProt-Databank [79]. The protein sequences with their respective UniProt IDs are listed in Table 4.

Table 4: Protein structures obtained from UniProt with their respective IDs.

Protein	**UniProt ID**
MHC-I gene Eqca-1*00101	Q30483
MHC-I genotype Eqca-N*00602	Q860N6
Horse β2m	P30441
Mouse β2m	P01887

Homology modeling

Homology models were prepared using MOE (version 2018.0101; Molecular Operating

Environment, Chemical Computing Group ULC, Montreal, Canada). The models were constructed using GB/VI scoring [80] with a maximum of ten main chain models. To check geometry of obtained homology models, Ramachandran (phi-psi angle) plots [44] were calculated with MOE.

The full MHC-I gene 3.1 model was prepared based on the hybrid equine α-chain - mouse β2m X-ray crystal structure with the best resolution (PDB-ID: 4ZUU [43]). The α-chain and β2m homology models were superposed onto the template. All side chain clashes were removed by energy minimization using the OPLS-AA force field [81], resulting in the full MHC-I gene 3.1 model. The complete model was relaxed in a MD simulation on settings described below.

Protein-Protein Docking

MHC-I-gD1 complex were prepared with MOE 2018 by protonation [82], modeling of missing side chains, deleting water molecules and charging termini. Protein - protein docking was performed using Rosetta 3 suite (version 2018-33) [83,84]. The orientations of MHC-I and gD were randomized (flags -randomize 1 -randomize 2) and spun (flag -spin) to the beginning of the docking process. Docking perturbation parameters were set to default: 3 Å translational and 8° rotational movement (flag -dock_pert 3 8) [85]. The residue side chains of both docking partners were allowed to rotate around the χ1 and the χ2 angles (flags -ex1 -ex2). In total 10 000 docking runs were conducted (flag -nstruct 10 000) as recommended by the Rosetta documentation [86], yielding over 7 000 poses in each docking round. A flat harmonic distance constraint between the Cα of MHC-I A173 and the gD backbone was added based on reported genotype studies indicating the pivotal role of MHC-I A173 [7,18]. This allowed us to limit the number of possible protein-protein docking complexes and perform local docking as recommended by the Rosetta documentation [86]. Constraint parameters were set to the default [86]: Distance 0 Å, standard deviation 1 Å and tolerance 5

597 Å to achieve the closest possible proximity between chains. In order to obtain a full MHC
598 peptide complex, peptide SDYVKVSNI, as used in cell-based assays, was manually fitted
599 into the MHC-I cleft. To fit our sequence, the peptide structure from the template (PDB-ID:
600 4ZUU) containing a nonapeptide CTSEEMNAF was superposed on the MHC-I homology
601 model. The co-crystallized nonapeptide sequence was manually mutated. The side chain
602 conformations were adjusted using MOE's rotamer tool and energy minimized using the
603 OPLS-AA force field to relax atomic clashes.
604 Finally, gD1 and gD4 were docked into the prepared MHC-peptide complex. In order to find
605 the final and most plausible docking pose of gD1 and gD4 in complex with MHC-I-peptide,
606 an in-house developed MD Analysis-based (version 0.19.2) [87,88] script was used to find
607 ionic key-contact defined as a distance of maximal 4.5 Å between Cγ atom of D261 in gD and
608 Cζ atom of R169 in MHC-I. The script was run in a Python 3.6 environment [89].
609

610 **Filtering of Docking Poses and Classification of Residues Involved in the**
611 **Protein-Protein Interface**

612 In order to filter the most plausible from all best-scored docking poses, we applied three rules
613 based on reported statistical evaluation of various protein-protein interactions (PPIs) [90,91]
614 and biological function of Herpesvirus gD (Table 5) [40]. The residues involved in the
615 protein-protein binding in the obtained binding hypotheses were classified according to the O-
616 ring theory (Figure 6) [90].
617

Table 5: Criteria applied in our analysis of protein-protein interfaces to filter the most energetically favored docking poses.

Filtering criterion	Rationale
Discarding docking poses with the C-	Orientation unlikely to be correct because

terminus participating in the resulting PPI	the C-terminus merges with a transmembrane-helix anchoring in viral membrane [40]
Discarding docking poses without lipophilic residues in the modeled PPI	Protein-protein interfaces with lipophilic contacts are common and entropically favored [91]
Accepting poses with contact to residues R, D, H, I, K, P, W, Y buried in interface areas	These residues are statistically enriched in protein-protein binding interfaces according to the O-ring theory [90]

Table 6: Classification of residues applied in our analysis of protein-protein interface.

Residue type in the binding interface	**Definition**
Hot spot residues	Amino acids statistically enriched in binding sites of protein - protein complexes and contributing more than 2 kcal/mol to the binding energy [90] or form lipophilic contacts [91]
O-ring	Residues preventing solvation of binding hot spots [90]

Binding pocket	Counterpart of hot spot residues on the surface of the binding partner.

Molecular Dynamics Simulations and Protein-Protein Interaction Analysis

Molecular Dynamics (MD) simulations were prepared using Maestro (version 11.7; Schrödinger, New York, USA) and carried out using Desmond 2018-3 (version 5.5) [92]. All systems were simulated on water-cooled GeForce RTX 2080 Ti graphics processing units (NVIDIA Corporation, Santa Clara, USA). The full MHC-I gene 3.1 homology model was solvated in a cubic box with 12 Å buffering with SPC water model [93]. The system was neutralized using sodium or chloride ions and osmotic pressure was adjusted with 0.15 M sodium chloride to achieve an isotonic system. The subsequent system relaxation was performed according to the default Desmond protocol. The MD simulation ran under periodic boundary conditions and as an NPT ensemble (constant particle number, pressure and temperature) using the OPLS 2005 force field [94]. The MD simulation was performed in one replicate over 100 ns. Coordinates of the relaxed model were retrieved after the backbone rmsd (**Error! Reference source not found.**A) had reached a stable plateau around 3 Å indicating protein equilibration.

Docking poses were simulated under the same conditions as the homology models. The movement of protein - protein complex hypotheses was observed in a single MD simulation over 100 ns resulting in ca. 5000 complex conformations. MD simulations of the final selected docking pose were performed in triplicates. The simulated systems contained around 140 000 – 168 500 atoms. The proteins were wrapped, aligned on the backbone and visually inspected in VMD [95] (version 1.9.3). Protein-protein interactions were analyzed using PyContact [46] (version 1.0.1) on default settings (distance cutoff 5.0 Å, angle cutoff 120.0° and distance cutoff between hydrogen and hydrogen bond acceptor of 2.5 Å). The PyContact

641 analysis was run in a Python 2.7 environment [89].

642

643 ## *In silico* modeling suggests low impact of MHC-I peptide on gD-MHC-I
644 ## binding

645 To test whether additional bias emerging from peptide modeling influenced docking
646 experiments, two docking rounds were performed. First, gD1 was docked to peptide-free
647 MHC-I. Second, gD1 was docked to MHC-I 3.1 homology model containing the peptide
648 SDYVKVSNI to check if docking provides comparable PPIs. Both docking rounds were
649 performed using the settings described above. As the initial filtering step, the ten highest
650 scored docking poses with the lowest Rosetta Energy were selected [96]. For further filtering,
651 the rules described in the Methods section were applied (Table 5). Four out of ten docking
652 poses fulfilled all three rules. Subsequently, single MD simulations for each docking pose
653 were performed to examine PPI stability. For all protein - protein complexes the backbone
654 rmsd was calculated to obtain an overview of the amplitude of protein movements. Only one
655 docking pose showed a nearly constant backbone rmsd value of 6 Å indicating low complex
656 movement (**Error! Reference source not found.** B). In order to characterize the obtained
657 PPI, we applied selection criteria and identified three residue patch-classes in the binding
658 surface as described in the Methods section (Figure 6). An inspection of the PPI over an MD
659 simulation trajectory with PyContact [46] (**Error! Reference source not found.**) revealed
660 two gD hot spot residues: D261 (surrounded by assumed gD O-ring T161, F213, and W257
661 and contacting binding pocket MHC-I residue R169 over whole simulation time) and W257
662 (surrounded by assumed O-ring R43, T161, and F213 and contacting binding pocket MHC-I
663 residue I166 over the whole trajectory). It can be concluded that PPIs of peptide-free and
664 peptide-bound docking poses are formed with similar residue patches (**Error! Reference**
665 **source not found.**, **Error! Reference source not found.**) suggesting that the presence of the
666 peptide in MHC-I does not influence gD binding. The key residue F213 is involved in both

667 PPIs indicating its importance. We observed that peptide-bound docking poses exploit larger
668 PPIs with more possible interactions than the peptide-free docking pose. We assume that
669 more contacts between gD and MHC-I are favorable for the binding. Therefore, peptide-
670 bound docking poses were chosen as the final ones.
671

672 # BAC mutagenesis

673 The point mutations F213A and D261N in EHV-1 and EHV-4 gDs were introduced via a two-
674 step Red recombination [47]. In brief, polymerase chain reaction (PCR) primers (**Error!**
675 **Reference source not found.**) were designed in a way that the 50 nucleotide recombinantion
676 arms include the point mutation and sequence to amplify the *kan*^{R} gene. For construction of
677 EHV-1-gD$_{D261N}$, EHV-1gD$_{F213A}$, EHV-4-gD$_{D261N}$, and EHV-4-gD$_{F213A}$ the primer pairs
678 VK61/VK62, VK63/VK64, VK65/VK66, and VK67/VK68 were used for PCR amplification
679 respectively. After Dpn-1 digest of PCR products, fragments were electroporated into GS1783
680 containing EHV-1 or EHV-4 BACs. DNA from Kanamycin resistant colonies was extracted
681 and correct mutants were selected based on Restriction fragment length polymorphism
682 (RFLP) using the restriction enzyme Pst-I. Correct clones were subjected to another round of
683 Red recombination to remove the *kan*^{R} gene. Final clones were further analyzed by RFLP and
684 sequencing, BAC extracted, puroified and transfected into 293T cells. Cells and supernatant
685 were harvested three days post transfection and used to infect ED cells. Revertants were
686 produced from mutant clones using the same procedure with primer pairs VK69/VK70,
687 VK71/VK72, VK73/VK74, and VK75/VK76 for producing EHV-1R-gD$_{D261N}$, EHV-1R-
688 gD$_{F213A}$, EHV-4R-gD$_{D261N}$, and EHV-4-RgD$_{F213A}$, respectively. All genotypes were confirmed
689 by PCR, RFLP, and Sanger sequencing using the primer pair WA2/VK8 and WA2/VK10
690 (**Error! Reference source not found.**) for EHV-1 and EHV-4 mutants, respectively.
691

692 # Western blotting

Western blot analysis was performed with soluble proteins: 50 µg/ml MHC-I, 5 µg/ml gD1, and 5 µg/ml gD4. Proteins were separated by 12% SDS-PAGE, transferred to a polyvinylidene difluoride (PVDF) membrane (Roth, Karlsruhe, Germany), detected with 1:1 000 dilution rabbit anti-His_6 (Sigma-Aldrich, St Louis, USA) antibody and 1:10 000 dilution goat anti-rabbit-HRP antibody (Sigma-Aldrich, St Louis, USA) and visualized by enhanced chemiluminescence (ECL Plus; Amersham).

Virus blocking assays

To block cell surface MHC-I, $1{,}5x10^5$ ED cells were seeded in 24-well plates. In the next day, cells were incubated with 20, 50, 100 or 150 µg/ml recombinant gD1, gD4 or $gD4_{36\text{-}280}$ for 1 h on ice. Subsequently cells were infected with either EHV-1 or EHV-4 at MOI=0.1 and incubated for 1 h at 37˚C. To remove un-penetrated viruses, cells were washed with citrate buffer, pH 3, containing 40 mM citric acid, 10 mM potassium chloride and 135 mM sodium chloride, then washed twice with phosphate buffered saline (PBS) and infection allowed to proceed for 24 h (EHV-1) or 48 h (EHV-4). For measurement of fluorescence intensity 10 000 cells were analyzed with a FACSCalibur flow cytometer (BD Biosciences) and the software CytExpert (Beckman Coulter, Krefeld). The experiment was repeated three independent times for each protein.

For plaque reduction assay the same protocol was applied for blocking surface MHC-I with minor changes. Cells were initially incubated with 150 µg/ml gD1 or gD4, infected with 100 PFU, and overlaid with 1.5% methylcellulose (Sigma-Aldrich, Taufkirchen, Germany) in Iscove's Modified Dulbecco's Medium (IMDM) after citrate treatment and washes with PBS. GFP plaques were counted after 48 h with a Zeiss Axiovert.A1 fluorescent microscope (Carl Zeiss AG, Jena, Germany). The experiment was repeated three independent times for each protein.

Virus growth kinetics

Virus replication was tested using multi-step growth kinetics and plaque areas were obtained as described before [50]. ED cells were grown to confluency in 24-well plates, infected with an MOI of 0.1 virus and incubated for 1 h at 37˚C. Viruses on the cell surface were removed by washing with citrate buffer. After neutralization with IMDM, cells were washed twice with PBS and finally overlaid with 500 µl IMDM. At indicated times after the citrate treatment cells and supernatant were collected separately for EHV-1 and together for EHV-4 and stored at -80˚C. Titers were determined by plating dilution series onto ED cells and counting plaque numbers after two days under a methylcellulose overlay. All plates were fixed for 10 min with 4% paraformaldehyde, washed with PBS and stained for 10 min with 0.1% crystal violet solution in PBS which was washed away with tab water. Viral titers are expressed as PFU per milliliter from three independent and blinded experiments.

Statistical analysis

For blocking assays, plaque numbers were normalized to infection levels without recombinant proteins. Statistical analysis was done using GraphPad Prism 5 software (San Diego, CA, USA) and one-way ANOVA Bonferroni's multiple comparison test, * indicates $P \leq 0.05$, ** indicates $P \leq 0.01$, *** indicates $P \leq 0.001$. Statistical analysis was done using an unpaired, one-tailed test. $P < 0.05$ was considered significant.

Acknowledgments

We acknowledge DESY (Hamburg, Germany), a member of the Helmholtz Association HGF, for the provision of experimental facilities. Diffraction data were collected at beamline P11 of the PETRA III storage ring (Hamburg, Germany) under proposal I-20180662, assisted by Eva Crosas, and at the beamlines of the BESSY II storage ring (Berlin, Germany) via the Joint Berlin MX-Laboratory sponsored by Helmholtz Zentrum Berlin für Materialien und Energie,

744 Freie Universität Berlin, Humboldt-Universität zu Berlin, Max-Delbrück-Centrum für
745 Molekulare Medizin, Leibniz-Forschungsinstitut für Molekulare Pharmakologie, Charité -
746 Universitätmedizin Berlin and Max-Planck-Institut für Kolloid- und Grenzflächenforschung.
747 We acknowledge David Machalz for providing us the MDAnalysis script allowing us fast
748 docking poses analysis and Jong-Heng Huang for performing MALS experiments. For mass
749 spectrometry (C.W.), we would like to acknowledge the assistance of the Core Facility
750 BioSupraMol.

751

752 References

753 [1] Osterrieder N, Van de Walle GR. Pathogenic potential of equine alphaherpesviruses: the
754 importance of the mononuclear cell compartment in disease outcome. Veterinary
755 Microbiology 2010;143:21–8.
756 [2] Cole NL, Grose C. Membrane fusion mediated by herpesvirus glycoproteins: the
757 paradigm of varicella-zoster virus. Reviews in Medical Virology 2003;13:207–22.
758 [3] Frampton AR, Stolz DB, Uchida H, Goins WF, Cohen JB, Glorioso JC. Equine
759 herpesvirus 1 enters cells by two different pathways, and infection requires the activation
760 of the cellular kinase ROCK1. Journal of Virology 2007;81:10879–89.
761 [4] Azab W, Gramatica A, Herrmann A, Osterrieder N. Binding of alphaherpesvirus
762 glycoprotein H to surface α4β1-integrins activates calcium-signaling pathways and
763 induces phosphatidylserine exposure on the plasma membrane. MBio 2015;6:e01552-15.
764 [5] Kurtz BM, Singletary LB, Kelly SD, Frampton AR. Equus caballus major
765 histocompatibility complex class I is an entry receptor for equine herpesvirus type 1.
766 Journal of Virology 2010;84:9027–34.
767 [6] Sasaki M, Hasebe R, Makino Y, Suzuki T, Fukushi H, Okamoto M, et al. Equine major
768 histocompatibility complex class I molecules act as entry receptors that bind to equine

769 herpesvirus-1 glycoprotein D. Genes to Cells 2011;16:343–57.
770 [7] Azab W, Harman R, Miller D, Tallmadge R, Frampton Jr AR, Antczak DF, et al. Equid
771 herpesvirus type 4 uses a restricted set of equine major histocompatibility complex class
772 I proteins as entry receptors. J Gen Virol 2014;95:1554–63.
773 [8] Triantafilou K, Fradelizi D, Wilson K, Triantafilou M. GRP78, a coreceptor for
774 coxsackievirus A9, interacts with major histocompatibility complex class I molecules
775 which mediate virus internalization. Journal of Virology 2002;76:633–43.
776 [9] Atwood WJ, Norkin LC. Class I major histocompatibility proteins as cell surface
777 receptors for simian virus 40. Journal of Virology 1989;63:4474–7.
778 [10] Norkin LC. Simian virus 40 infection via MHC class I molecules and caveolae.
779 Immunological Reviews 1999;168:13–22.
780 [11] Hong SS, Karayan L, Tournier J, Curiel DT, Boulanger PA. Adenovirus type 5 fiber
781 knob binds to MHC class I α2 domain at the surface of human epithelial and B
782 lymphoblastoid cells. The EMBO Journal 1997;16:2294–306.
783 [12] Mullen MM, Haan KM, Longnecker R, Jardetzky TS. Structure of the Epstein-Barr virus
784 gp42 protein bound to the MHC class II receptor HLA-DR1. Molecular Cell
785 2002;9:375–85.
786 [13] David-Watine B, Israël A, Kourilsky P. The regulation and expression of MHC class I
787 genes. Immunology Today 1990;11:286–92.
788 [14] Tallmadge RL, Campbell JA, Miller DC, Antczak DF. Analysis of MHC class I genes
789 across horse MHC haplotypes. Immunogenetics 2010;62:159–72.
790 [15] Gilcrease MZ. Integrin signaling in epithelial cells. Cancer Letters 2007;247:1–25.
791 [16] Bjorkman PJ, Parham P. Structure, function, and diversity of class I major
792 histocompatibility complex molecules. Annual Review of Biochemistry 1990;59:253–
793 88.
794 [17] Germain RN, Margulies DH. The biochemistry and cell biology of antigen processing

795 and presentation. Annual Review of Immunology 1993;11:403–50.
796 [18] Sasaki M, Kim E, Igarashi M, Ito K, Hasebe R, Fukushi H, et al. Single amino acid
797 residue in the A2 domain of major histocompatibility complex class I is involved in the
798 efficiency of equine herpesvirus-1 entry. Journal of Biological Chemistry
799 2011;286:39370–8.
800 [19] Ellis S, Martin A, Holmes E, Morrison W. At least four MHC class I genes are
801 transcribed in the horse: phylogenetic analysis suggests an unusual evolutionary history
802 for the MHC in this species. International Journal of Immunogenetics 1995;22:249–60.
803 [20] Patel J, Heldens J. Equine herpesviruses 1 (EHV-1) and 4 (EHV-4)–epidemiology,
804 disease and immunoprophylaxis: a brief review. The Veterinary Journal 2005;170:14–
805 23.
806 [21] Kydd JH, Townsend HG, Hannant D. The equine immune response to equine
807 herpesvirus-1: the virus and its vaccines. Veterinary Immunology and Immunopathology
808 2006;111:15–30.
809 [22] Allen G. Molecular epizootiology, pathogenesis, and prophylaxis of equine herpesvirus-
810 1 infections. Prog Vet Microbiol Immunol 1986;2:78–144.
811 [23] Burrows R, Goodridge D. In vivo and in vitro studies of equine rhinopneumonitis virus
812 strains. Equine Infectious Diseases, Karger Publishers; 1974, p. 306–21.
813 [24] Goehring L, Wagner B, Bigbie R, Hussey S, Rao S, Morley P, et al. Control of EHV-1
814 viremia and nasal shedding by commercial vaccines. Vaccine 2010;28:5203–11.
815 [25] Goodman LB, Wimer C, Dubovi EJ, Gold C, Wagner B. Immunological correlates of
816 vaccination and infection for equine herpesvirus 1. Clin Vaccine Immunol 2012;19:235–
817 41.
818 [26] Krummenacher C, Supekar VM, Whitbeck JC, Lazear E, Connolly SA, Eisenberg RJ, et
819 al. Structure of unliganded HSV gD reveals a mechanism for receptor-mediated
820 activation of virus entry. The EMBO Journal 2005;24:4144–53.

821 [27] Yue D, Chen Z, Yang F, Ye F, Lin S, He B, et al. Crystal structure of bovine herpesvirus
822 1 glycoprotein D bound to nectin-1 reveals the basis for its low-affinity binding to the
823 receptor. Science Advances 2020;6:5147.
824 [28] Lu G, Zhang N, Qi J, Li Y, Chen Z, Zheng C, et al. Crystal structure of herpes simplex
825 virus 2 gD bound to nectin-1 reveals a conserved mode of receptor recognition. Journal
826 of Virology 2014;88:13678–88.
827 [29] Li A, Lu G, Qi J, Wu L, Tian K, Luo T, et al. Structural basis of nectin-1 recognition by
828 pseudorabies virus glycoprotein D. PLoS Pathogens 2017;13:e1006314.
829 [30] Matsumoto H, Haniu H, Komori N. Determination of protein molecular weights on
830 SDS-PAGE. Electrophoretic Separation of Proteins, Springer; 2019, p. 101–5.
831 [31] Flowers CC, Eastman EM, O'Callaghan DJ. Sequence analysis of a glycoprotein D gene
832 homolog within the unique short segment of the EHV-1 genome. Virology
833 1991;180:175–84.
834 [32] Carfi A, Willis SH, Whitbeck JC, Krummenacher C, Cohen GH, Eisenberg RJ, et al.
835 Herpes simplex virus glycoprotein D bound to the human receptor HveA. Molecular Cell
836 2001;8:169–79.
837 [33] Adams PD, Afonine PV, Bunkóczi G, Chen VB, Davis IW, Echols N, et al. PHENIX: a
838 comprehensive Python-based system for macromolecular structure solution. Acta
839 Crystallographica Section D: Biological Crystallography 2010;66:213–21.
840 [34] Chen VB, Arendall WB, Headd JJ, Keedy DA, Immormino RM, Kapral GJ, et al.
841 MolProbity: all-atom structure validation for macromolecular crystallography. Acta
842 Crystallographica Section D: Biological Crystallography 2010;66:12–21.
843 [35] Connolly SA, Whitbeck JC, Rux AH, Krummenacher C, Cohen GH, Eisenberg RJ, et al.
844 Glycoprotein D homologs in herpes simplex virus type 1, pseudorabies virus, and bovine
845 herpes virus type 1 bind directly to human HveC (nectin-1) with different affinities.
846 Virology 2001;280:7–18.

847 [36] Willis SH, Rux AH, Peng C, Whitbeck JC, Nicola AV, Lou H, et al. Examination of the
848 kinetics of herpes simplex virus glycoprotein D binding to the herpesvirus entry
849 mediator, using surface plasmon resonance. Journal of Virology 1998;72:5937–47.
850 [37] Whitbeck JC, Muggeridge MI, Rux AH, Hou W, Krummenacher C, Lou H, et al. The
851 major neutralizing antigenic site on herpes simplex virus glycoprotein D overlaps a
852 receptor-binding domain. Journal of Virology 1999;73:9879–90.
853 [38] Rux AH, Willis SH, Nicola AV, Hou W, Peng C, Lou H, et al. Functional region IV of
854 glycoprotein D from herpes simplex virus modulates glycoprotein binding to the
855 herpesvirus entry mediator. Journal of Virology 1998;72:7091–8.
856 [39] Krummenacher C, Rux AH, Whitbeck JC, Ponce-de-Leon M, Lou H, Baribaud I, et al.
857 The first immunoglobulin-like domain of HveC is sufficient to bind herpes simplex virus
858 gD with full affinity, while the third domain is involved in oligomerization of HveC.
859 Journal of Virology 1999;73:8127–37.
860 [40] Zhang N, Yan J, Lu G, Guo Z, Fan Z, Wang J, et al. Binding of herpes simplex virus
861 glycoprotein D to nectin-1 exploits host cell adhesion. Nature Communications
862 2011;2:577.
863 [41] Rudolph J, O'CALLAGHAN D, Osterrieder N. Cloning of the genomes of equine
864 herpesvirus type 1 (EHV-1) strains KyA and RacL11 as bacterial artificial chromosomes
865 (BAC). Journal of Veterinary Medicine, Series B 2002;49:31–6.
866 [42] Azab W, Kato K, Arii J, Tsujimura K, Yamane D, Tohya Y, et al. Cloning of the
867 genome of equine herpesvirus 4 strain TH20p as an infectious bacterial artificial
868 chromosome. Archives of Virology 2009;154:833–42.
869 [43] Yao S, Liu J, Qi J, Chen R, Zhang N, Liu Y, et al. Structural illumination of equine
870 MHC class I molecules highlights unconventional epitope presentation manner that is
871 evolved in equine leukocyte antigen alleles. The Journal of Immunology
872 2016;196:1943–54.

873 [44] Ramachandran GN. Stereochemistry of polypeptide chain configurations. J Mol Biol
874 1963;7:95–9.
875 [45] Honig B, Nicholls A. Classical electrostatics in biology and chemistry. Science
876 1995;268:1144–9.
877 [46] Scheurer M, Rodenkirch P, Siggel M, Bernardi RC, Schulten K, Tajkhorshid E, et al.
878 PyContact: Rapid, customizable, and visual analysis of noncovalent interactions in MD
879 simulations. Biophysical Journal 2018;114:577–83.
880 [47] Tischer KB, von Einem J, Kaufer B, Osterrieder N. Two-step red-mediated
881 recombination for versatile high-efficiency markerless DNA manipulation in Escherichia
882 coli. Biotechniques 2006;40:191–7.
883 [48] Osterrieder N. Construction and characterization of an equine herpesvirus 1 glycoprotein
884 C negative mutant. Virus Research 1999;59:165–77.
885 [49] Spear PG, Longnecker R. Herpesvirus entry: an update. Journal of Virology
886 2003;77:10179–85.
887 [50] Azab W, Tsujimura K, Maeda K, Kobayashi K, Mohamed YM, Kato K, et al.
888 Glycoprotein C of equine herpesvirus 4 plays a role in viral binding to cell surface
889 heparan sulfate. Virus Research 2010;151:1–9.
890 [51] Csellner H, Walker C, Wellington J, McLure L, Love D, Whalley J. EHV-1 glycoprotein
891 D (EHV-1 gD) is required for virus entry and cell-cell fusion, and an EHV-1 gD deletion
892 mutant induces a protective immune response in mice. Archives of Virology
893 2000;145:2371–85.
894 [52] Azab W, Zajic L, Osterrieder N. The role of glycoprotein H of equine herpesviruses 1
895 and 4 (EHV-1 and EHV-4) in cellular host range and integrin binding. Veterinary
896 Research 2012;43:61.
897 [53] Azab W, Osterrieder K. Initial contact: the first steps in herpesvirus entry. Cell Biology
898 of Herpes Viruses, Springer; 2017, p. 1–27.

899 [54] Lazear E, Carfi A, Whitbeck JC, Cairns TM, Krummenacher C, Cohen GH, et al.
900 Engineered disulfide bonds in herpes simplex virus type 1 gD separate receptor binding
901 from fusion initiation and viral entry. Journal of Virology 2008;82:700–9.
902 [55] Di Giovine P, Settembre EC, Bhargava AK, Luftig MA, Lou H, Cohen GH, et al.
903 Structure of herpes simplex virus glycoprotein D bound to the human receptor nectin-1.
904 PLoS Pathogens 2011;7:e1002277.
905 [56] Manoj S, Jogger CR, Myscofski D, Yoon M, Spear PG. Mutations in herpes simplex
906 virus glycoprotein D that prevent cell entry via nectins and alter cell tropism.
907 Proceedings of the National Academy of Sciences 2004;101:12414–21.
908 [57] Handler CG, Cohen GH, Eisenberg RJ. Cross-linking of glycoprotein oligomers during
909 herpes simplex virus type 1 entry. Journal of Virology 1996;70:6076–82.
910 [58] Krummenacher C, Carfí A, Eisenberg RJ, Cohen GH. Entry of herpesviruses into cells:
911 the enigma variations. Viral entry into host cells, Springer; 2013, p. 178–95.
912 [59] Studdert M, Blackney M. Equine herpesviruses: on the differentiation of respiratory
913 from foetal strains of type 1. Australian Veterinary Journal 1979;55:488–92.
914 [60] Ahn BC, Zhang Y, O'Callaghan DJ. The equine herpesvirus-1 (EHV-1) IR3 transcript
915 downregulates expression of the IE gene and the absence of IR3 gene expression alters
916 EHV-1 biological properties and virulence. Virology 2010;402:327–37.
917 [61] Greenwood AD, Tsangaras K, Ho SY, Szentiks CA, Nikolin VM, Ma G, et al. A
918 potentially fatal mix of herpes in zoos. Current Biology 2012;22:1727–31.
919 [62] Abdelgawad A, Hermes R, Damiani A, Lamglait B, Czirják GÁ, East M, et al.
920 Comprehensive serology based on a peptide ELISA to assess the prevalence of closely
921 related equine herpesviruses in zoo and wild animals. PLoS One 2015;10:e0138370.
922 [63] Abdelgawad A, Azab W, Damiani AM, Baumgartner K, Will H, Osterrieder N, et al.
923 Zebra-borne equine herpesvirus type 1 (EHV-1) infection in non-African captive
924 mammals. Veterinary Microbiology 2014;169:102–6.

925 [64] Azab W, Kato K, Abdel-Gawad A, Tohya Y, Akashi H. Equine herpesvirus 4: Recent
926 advances using BAC technology. Veterinary Microbiology 2011;150:1–14.
927 [65] Santos KF, Jovin SM, Weber G, Pena V, Lührmann R, Wahl MC. Structural basis for
928 functional cooperation between tandem helicase cassettes in Brr2-mediated remodeling
929 of the spliceosome. Proceedings of the National Academy of Sciences 2012;109:17418–
930 23.
931 [66] Kabsch W. Xds. Acta Crystallographica Section D: Biological Crystallography
932 2010;66:125–32.
933 [67] Bunkóczi G, Echols N, McCoy AJ, Oeffner RD, Adams PD, Read RJ. Phaser. MRage:
934 automated molecular replacement. Acta Crystallographica Section D: Biological
935 Crystallography 2013;69:2276–86.
936 [68] Emsley P, Lohkamp B, Scott WG, Cowtan K. Features and development of Coot. Acta
937 Crystallographica Section D: Biological Crystallography 2010;66:486–501.
938 [69] Afonine PV, Grosse-Kunstleve RW, Echols N, Headd JJ, Moriarty NW, Mustyakimov
939 M, et al. Towards automated crystallographic structure refinement with phenix. refine.
940 Acta Crystallographica Section D: Biological Crystallography 2012;68:352–67.
941 [70] Williams CJ, Headd JJ, Moriarty NW, Prisant MG, Videau LL, Deis LN, et al.
942 MolProbity: More and better reference data for improved all-atom structure validation.
943 Protein Science 2018;27:293–315.
944 [71] Yang H, Guranovic V, Dutta S, Feng Z, Berman HM, Westbrook JD. Automated and
945 accurate deposition of structures solved by X-ray diffraction to the Protein Data Bank.
946 Acta Crystallographica Section D: Biological Crystallography 2004;60:1833–9.
947 [72] Kabsch W, Sander C. DSSP: definition of secondary structure of proteins given a set of
948 3D coordinates. Biopolymers 1983;22:2577–637.
949 [73] Sievers F, Wilm A, Dineen D, Gibson TJ, Karplus K, Li W, et al. Fast, scalable
950 generation of high-quality protein multiple sequence alignments using Clustal Omega.

951 Molecular Systems Biology 2011;7.

952 [74] Barton GJ, others. ALSCRIPT: a tool to format multiple sequence alignments. Protein

953 Engineering Design and Selection 1993;6:37–40.

954 [75] DeLano WL. PyMOL 2002.

955 [76] Tarazona MP, Saiz E. Combination of SEC/MALS experimental procedures and

956 theoretical analysis for studying the solution properties of macromolecules. Journal of

957 Biochemical and Biophysical Methods 2003;56:95–116.

958 [77] Dey P, Bergmann T, Cuellar-Camacho JL, Ehrmann S, Chowdhury MS, Zhang M, et al.

959 Multivalent Flexible Nanogels Exhibit Broad-Spectrum Antiviral Activity by Blocking

960 Virus Entry. ACS Nano 2018;12:6429–42.

961 [78] Schasfoort RB. Handbook of surface plasmon resonance. Royal Society of Chemistry;

962 2017.

963 [79] Consortium U. UniProt: a worldwide hub of protein knowledge. Nucleic Acids Research

964 2019;47:D506–15.

965 [80] Labute P. The generalized Born/volume integral implicit solvent model: estimation of

966 the free energy of hydration using London dispersion instead of atomic surface area.

967 Journal of Computational Chemistry 2008;29:1693–8.

968 [81] Kaminski GA, Friesner RA, Tirado-Rives J, Jorgensen WL. Evaluation and

969 reparametrization of the OPLS-AA force field for proteins via comparison with accurate

970 quantum chemical calculations on peptides. The Journal of Physical Chemistry B

971 2001;105:6474–87.

972 [82] Labute P. Protonate3D: assignment of ionization states and hydrogen coordinates to

973 macromolecular structures. Proteins: Structure, Function, and Bioinformatics

974 2009;75:187–205.

975 [83] Gray JJ, Moughon S, Wang C, Schueler-Furman O, Kuhlman B, Rohl CA, et al.

976 Protein–protein docking with simultaneous optimization of rigid-body displacement and

977 side-chain conformations. Journal of Molecular Biology 2003;331:281–99.
978 [84] Sircar A, Chaudhury S, Kilambi KP, Berrondo M, Gray JJ. A generalized approach to
979 sampling backbone conformations with RosettaDock for CAPRI rounds 13–19. Proteins:
980 Structure, Function, and Bioinformatics 2010;78:3115–23.
981 [85] Chaudhury S, Gray JJ. Conformer selection and induced fit in flexible backbone
982 protein–protein docking using computational and NMR ensembles. Journal of Molecular
983 Biology 2008;381:1068–87.
984 [86] Weitzner J BB,M; Kilambi, K; Thottungal, R; Chaudhury, S; Wang, C; Gray. Docking
985 Protocol (RosettaDock). 2017.
986 [87] Gowers RJ, Linke M, Barnoud J, Reddy TJE, Melo MN, Seyler SL, et al. MDAnalysis: a
987 Python package for the rapid analysis of molecular dynamics simulations. Los Alamos
988 National Lab.(LANL), Los Alamos, NM (United States); 2019.
989 [88] Michaud-Agrawal N, Denning EJ, Woolf TB, Beckstein O. MDAnalysis: a toolkit for
990 the analysis of molecular dynamics simulations. Journal of Computational Chemistry
991 2011;32:2319–27.
992 [89] van Rossum G. Python tutorial, Technical Report CS-R9526, Centrum voor Wiskunde
993 en Informatica (CWI), Amsterdam." 1995.
994 [90] Bogan AA, Thorn KS. Anatomy of hot spots in protein interfaces. Journal of Molecular
995 Biology 1998;280:1–9.
996 [91] Liu Q, Li J. Protein binding hot spots and the residue-residue pairing preference: a water
997 exclusion perspective. BMC Bioinformatics 2010;11:244.
998 [92] Bowers KJ, Chow DE, Xu H, Dror RO, Eastwood MP, Gregersen BA, et al. Scalable
999 algorithms for molecular dynamics simulations on commodity clusters. SC'06:
1000 Proceedings of the 2006 ACM/IEEE Conference on Supercomputing, IEEE; 2006, p.
1001 43–43.
1002 [93] Toukan K, Rahman A. Molecular-dynamics study of atomic motions in water. Physical

1003 Review B 1985;31:2643.

1004 [94] Banks JL, Beard HS, Cao Y, Cho AE, Damm W, Farid R, et al. Integrated modeling

1005 program, applied chemical theory (IMPACT). Journal of Computational Chemistry

1006 2005;26:1752–80.

1007 [95] Humphrey W, Dalke A, Schulten K, others. VMD: visual molecular dynamics. Journal

1008 of Molecular Graphics 1996;14:33–8.

1009 [96] Chaudhury S, Berrondo M, Weitzner BD, Muthu P, Bergman H, Gray JJ. Benchmarking

1010 and analysis of protein docking performance in Rosetta v3. 2. PloS One 2011;6:e22477.

1011

Figures

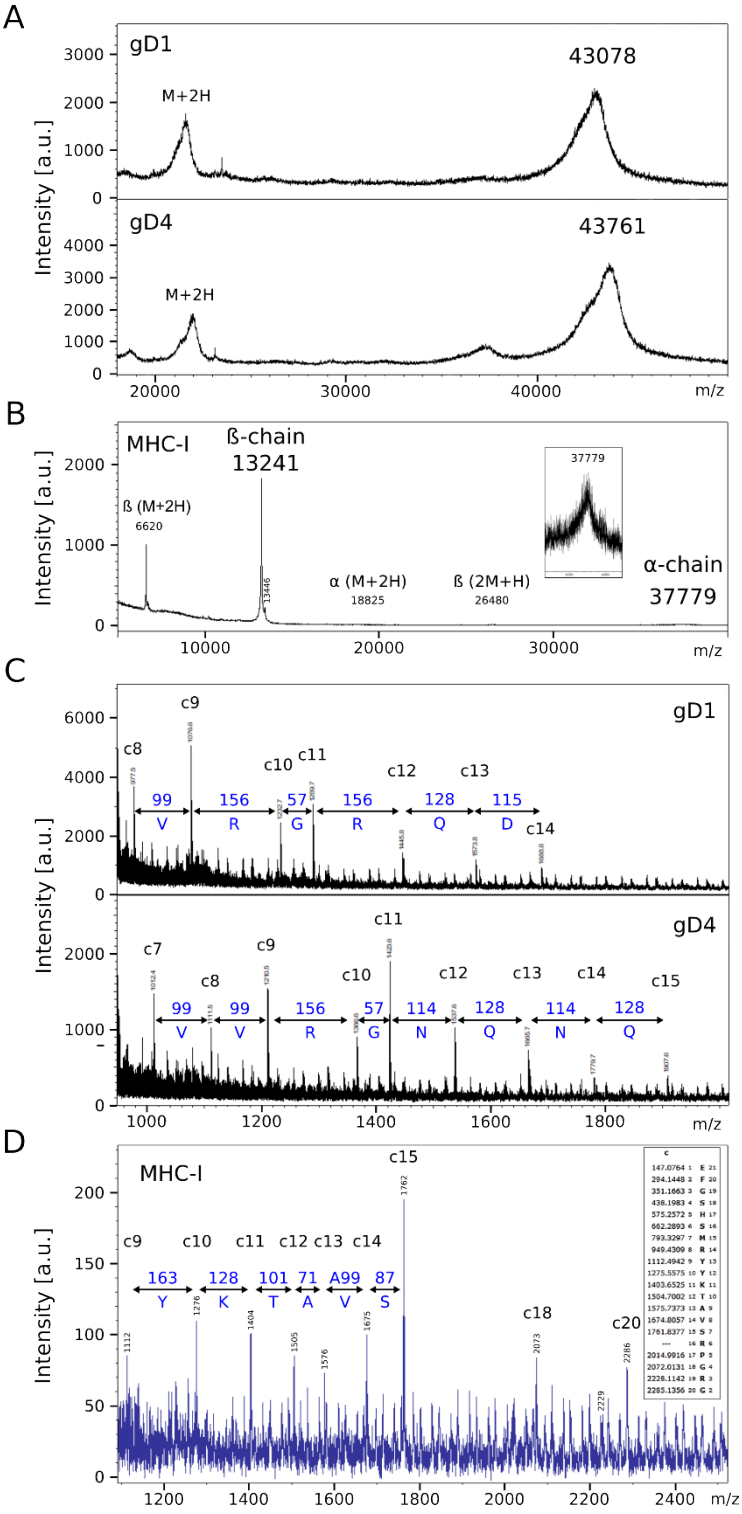

Figure 1: Mass spectrometric analysis of gD1 and gD4.

(A) Intact protein mass analysis of recombinant gD1 (top) and gD4 (bottom) including N-terminal residues (EF: glutamic acid and phenylalanine) from *Eco*RI restriction site, TEV

cleavage site and His_6-tag on sinapinic acid (SA) matrix. (B) Intact protein mass analysis of recombinant MHC-I complex comprised of β2m and MHC-I-α-chain (insert zoom) including the same additional residues as gD1 and gD4. (C) In-source decay (ISD) spectra of recombinant gD1 (top), gD4 (bottom), and (D) MHC-I to ascertain the correct N-termini, insert: Theoretical c-ion series including the N-terminal EF extension.

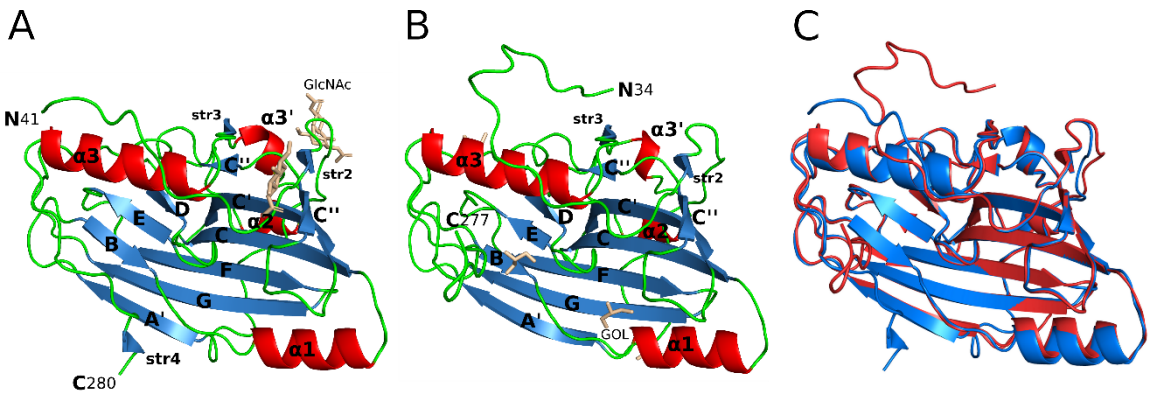

Figure 2: Crystal structure comparison of gD1 and gD4.

Cartoon representation of (A) gD1 (2.45 Å resolution, PDB-ID: 6SQJ) and (B) gD4 (1.9 Å resolution, PDB-ID: 6TM8) monomer crystal structures. Molecule orientation is identical and secondary structures were assigned with dssp [72]. Helices are displayed in red, sheets in blue, and loops in green. N-acetylglucosamine (GlcNAc) and glycerol (GOL) molecules are shown in stick representation in beige. (C) Superposition of the crystal structures of gD1 (blue, PDB-ID 6SQJ) and gD4 (red, PDB-ID 6TM8). GlcNAc and glycerol molecules are not shown.

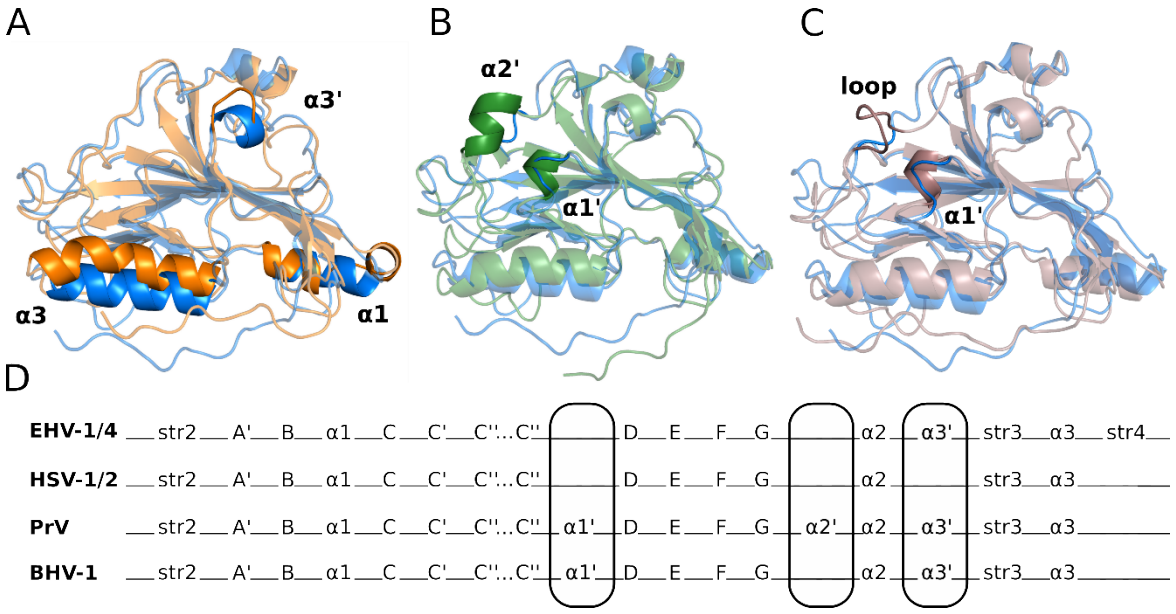

1032

Figure 3: Glycoprotein D from alphaherpesviruses have a similar crystal and secondary structure.

Superposition of crystal structures in cartoon representation of gD from EHV-1 (blue, PDB-ID 6SQJ) with (A) HSV-1 (orange, PDB-ID 2C36), (B) PrV (green, PDB-ID 5X5V), and (C) BoHV-1 (brown, PDB-ID 6LS9) gD. Main differences in global fold are highlighted. (D) Comparison of secondary structure elements of EHV-1/4, HSV-1/2, PrV, and BoHV-1 gD. Main differences in global fold are encircled.

1033

1034

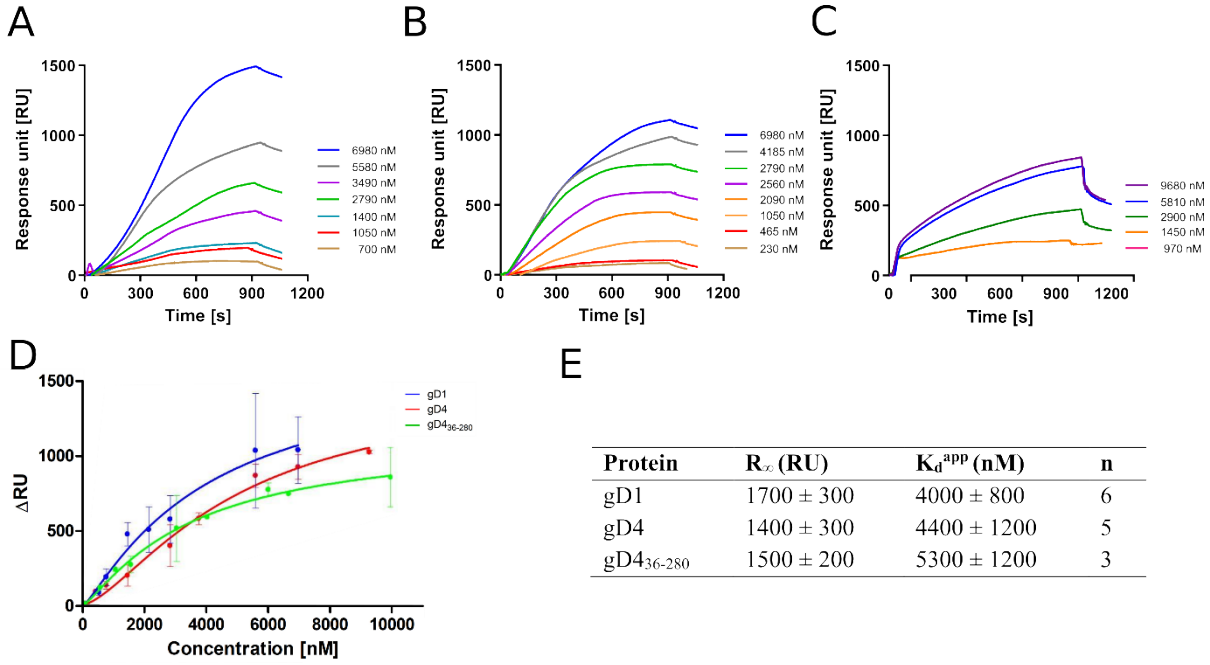

Protein	R_∞ (RU)	K_d^{app} (nM)	n
gD1	1700 ± 300	4000 ± 800	6
gD4	1400 ± 300	4400 ± 1200	5
$gD4_{36-280}$	1500 ± 200	5300 ± 1200	3

Figure 4: Binding affininties of gD1, gD4 and $gD4_{36-280}$ to the entry receptor MHC-I are in micro molar range.

(A, B, C) Representative SPR sensorgram profiles of recombinant gDs binding to amine-coupled recombinant MHC-I. Data were collected for several independent experiments [(A) gD1 n=6, (B) gD4 n=5, (C) $gD4_{36-280}$ n=3). (D) Binding curves for different gD concentrations from at least three independent experiments. Displayed are means with standard deviation (SD). The solid lines represent a fit of a Hill-Wand model to the data. (E) Parameters obtained from SPR binding curves of gD1, gD4, and gD436-280. R∞ is the maximum signal obtained from the bound protein; K_d^{app} is the apparent equilibrium dissociation constant, n corresponds to the number of independent experiments.

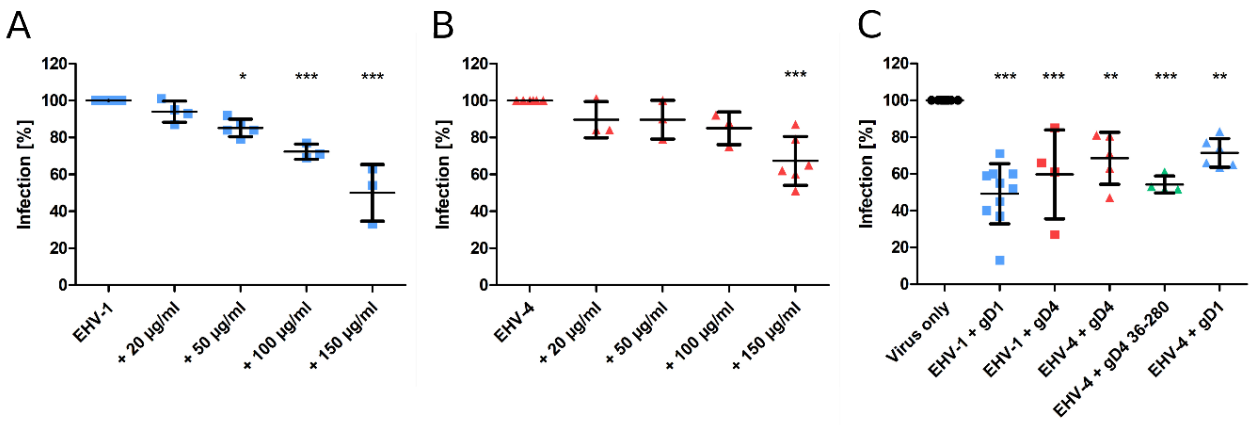

Figure 5: Recombinant gD1, gD4 and $gD4_{36-280}$ blocks EHV-1 and EHV-4 infection in ED cells.

(A) EHV-1 and (B) EHV-4 virus entry into ED cells blocked by different concentrations of gD1 and 4, respectively, and analyzed by flow cytometry. Cells were incubated with soluble proteins for 1 h on ice and infected with either EHV-1 or EHV-4 at MOI = 0.1. After 1 h, viruses on the cell surface were removed with citrate buffer and GFP levels were analyzed after 24-48 h by flow cytometry. (C) Plaque reduction assay of EHV-1and EHV-4 with recombinant protein. ED cells were incubated for 1 h on ice with 150 µg/ml gD1, gD4 or $gD4_{36-280}$ and infected with 100 PFU of each virus. After 1 h, viruses on the cell surface were removed with citrate buffer and cells were overlaid with methylcellulose. GFP plaques were counted after 48 h. The experiment was repeated independently three times for each protein. Plaque numbers were normalized to infection levels without recombinant proteins. Statistical analysis was done using one-way ANOVA Bonferroni's multiple comparison test, * indicates $P \leq 0.05$, ** indicates $P \leq 0.01$, *** indicates $P \leq 0.001$. Error bars represent mean with SD.

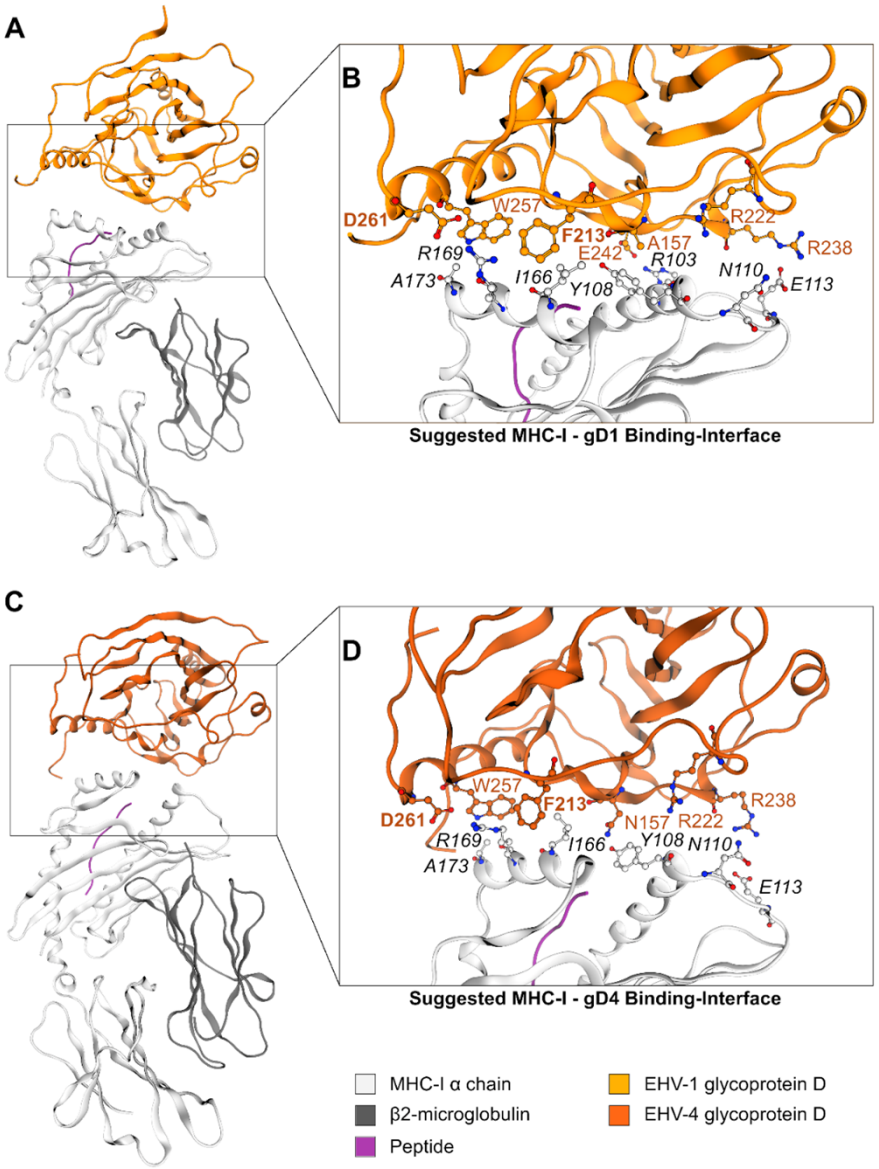

1050

Figure 6: The gD1- and gD4-MHC-I interface.

(A) Suggested model of the MHC-I – gD1 complex and (B) detailed view on the hypothesized binding interface. (C) Suggested model of the MHC-I – gD4 complex and (D) detailed view on the hypothesized binding interface. EHV gD residues are highlighted in orange and hot spot residues additionally in bold font. Color-code: grey ribbon – MHC-I, dark grey ribbon – β2m, orange ribbon – gD1, dark orange ribbon – gD4, purple ribbon – peptide, grey/orange balls – carbon atoms, blue balls – nitrogen atoms, red balls – oxygen atoms.

1051

1052

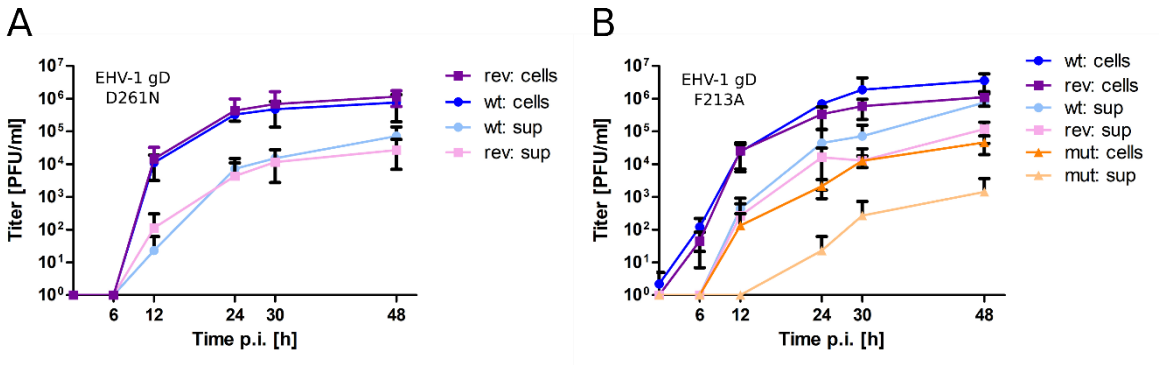

Figure 7: Mutating gD1 residues D261N and F213A impairs EHV-1 growth in ED cells.

Multi-step growth kinetics of EHV-1 parental virus and gD mutants. ED cells were infected with an MOI of 0.01, cells and supernatant were collected separately at indicated time points post infection and titrated on ED cells. Shown are means with standard deviation (SD) of three independent experiments. (A) EHV-1 parental virus (blue colors) and EHV-1-gD_{D261N} (violet colors). (B) EHV-1 parental virus (blue colors), EHV-1-gD_{F213A} (orange colors) and EHV-1-gD-$_{F213A}$ (violet colors).

1053

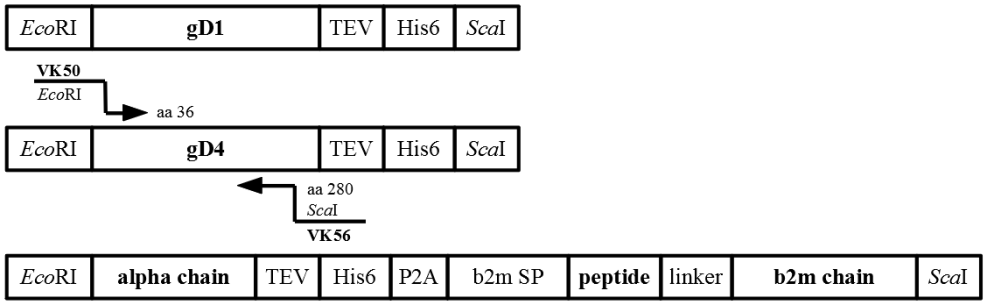

Figure 8: Synthetic genes used for cloning.

Schematic representation of synthetic genes for protein production of gD1, gD4, equine MHC-I 3.1 with cloning strategy for gD436-280.

Supporting information

Figure S 1: SDS-PAGE and western blot of MHC-I, gD1, and gD4. (A) Coomassie stained SDS-PAGE on 12% gel. For MHC-I, only the α-chain is visible in (A) and (B). M = marker. (B) Western blot: MHC-I (50 µg/ml), gD1 (5 µg/ml), and gD4 (5 µg/ml) detected with 1:1000 rabbit anti-His_6 antibody and 1:10000 goat anti-rabbit-HRP as secondary antibody.

Figure S 2: Protein purification by size exclusion chromatography (SEC). Representative SEC curves of concentrated (A) gD1, (B) gD4, (C) $gD4_{36\text{-}280}$, and (D) MHC-I run on Superdex 200 16/600 after purification through immobilized metal ion affinity chromatography (IMAC). Solid curves show UV absorbance at 280nm and the dotted curves at 260nm.

Figure S 3: SDS-PAGE of protein purification by size exclusion chromatography (SEC). Representative size exclusion chromatography (SEC) fractions of proteins produced in insect cells on Coomassie stained 12% sodium dodecyl sulfate (SDS) gels. (A) gD1 (approximately 43 kDa), (B) gD4 (approximately 43 kDa), (C) $gD4_{36\text{-}280}$ (approximately 30 kDa), and (D) MHC-I (comprised of α-chain with an approximate size of 38 kDa and β2m (with the linker and peptide) with an approximate size of 13 kDa). M = marker, FT = flow through affinity chromatography, E = elution affinity chromatography, L = loaded on SEC column.

Figure S 4: Tandem mass spectrometry (MS/MS) of in-gel digested gD1 and gD4. Exemplary spectra are shown which confirm the identity of the analyzed proteins and the integrity of their termini. The inserts display the theoretical b and y fragments ions. (A) N-terminal peptide of gD1 generated by cleavage with Asp-N endoproteinase (M+H= 1574.90, pos. 001-013, sequence EFEKAKRAVRGRQ.D); (B) N-terminal peptide of gD4 obtained by trypsin cleavage (M+H=1013.52, pos. 001-007, sequence EFENYRR); (C) C-terminal peptide of gD4 including the His_6-tag, generated by Glu-C endoproteinase (M+H=1563.74, pos. 323-334, sequence ENLYFQG-H_6).

Figure S 5: *S*ize exclusion chromatography (SEC) combined with multi-angle static light scattering (MALS) analysis of gD1.

The gD1 crystal structure consists of a homodimer with two ions interpreted as magnesium originating from the crystallization solution, trapped between them. The ionic interaction together with a high Complex Formation Significance Score of 0.765 (PDB Proteins, Interfaces, Structures and Assemblies (PISA) server www.ebi.ac.uk/pdbe/pisa/) suggested that gD1 might form a dimer on the virus envelope as has been proposed for HSV-1 gD [26]. To evaluate whether recombinant gD of EHV-1 has a homodimeric and/or monomeric form in solution, molecular mass calculation based on SEC-MALS analysis was performed for gD1. Green curve represents the normalized refractive index trace (intensity, right y-axis) for gD1 eluted from a Superdex 200 10/300 column. Blue line under the peak corresponds to the averaged molecular mass distribution (left y axis) across the peak. Exclusively the monomeric form with an approximate molecular weight of 44 kDa was detected. It can be concluded that gD1 is a monomer in solution.

Figure S 6: Sequence alignment of EHV-1 with HSV-1 and PrV. Sequence alignment based on secondary structures of gD1 with (A) HSV-1 (PDB ID 2C3A) and (B) PrV (PDB ID 5X5V) gD according to dssp [72]. Sheets are indicated as pink arrows, helices as blue cylinder, disulfide bonds as yellow boxes, glycosylation sites in gD1 as green dots, and magnesium coordinating residues in gD1 as purple dots. Labels correspond to the naming scheme presented by Li et al. [29].

Figure S 7: Ramachandran plots for modeled MHC-I. Ramachandran plots for (A) MHC-I (gene 3.1) and (B) equine β2m. Symbol code: green point-residue with favorable geometry, yellow point- residue with allowed geometry.